International Atomic Energy Agency

INDC(NDS)- 310

INDC INTERNATIONAL NUCLEAR DATA COMMITTEE

Particle Interchange Reactions Involving Plasma Impurity Ions and H_2, D_2 and HD

P. B. Armentrout* C. Illescas#† and J. Botero#

*Department of Chemistry, University of Utah, Salt Lake City, Utah, USA

International Atomic Energy Agency, P.O. Box 100, A-1400 Vienna, Austria

† Departamento de Química, CIX, Universidad Autónoma de Madrid, Cantoblanco,E-28049, Spain

Vienna, January, 1995

IAEA NUCLEAR DATA SECTION, WAGRAMERSTRASSE 5, A-1400 VIENNA

INDC(NDS)- 310

Particle Interchange Reactions Involving Plasma Impurity Ions and H_2, D_2 and HD

P. B. Armentrout* C. Illescas#† and J. Botero#

*Department of Chemistry, University of Utah, Salt Lake City, Utah, USA

International Atomic Energy Agency, P.O. Box 100, A-1400 Vienna, Austria

† Departamento de Química, CIX, Universidad Autónoma de Madrid, Cantoblanco,E-28049, Spain

Vienna, January, 1995

Abstract

The kinetic energy dependence of the cross section of particle interchange reactions between a variety of plasma impurities (C^+, O^+, Si^+, Ti^+, V^+, Cr^+, Fe^+, Ni^+, Cu^+, Al^+, Mo^+, Mn^+, Mg^+, B^+, Si^+, Ge^+, Nb^+, Ag^+, Ne^+, Ar^+ and Kr^+) and the main plasma constituents, in molecular state (H_2, D_2 and HD), of a thermonuclear fusion device are reviewed. Most of the experimental results presented here were obtained with a guided ion beam mass spectromter. Analytic fits to the data are presented for most cases.

Contents

1 Introduction **1**

2 Experimental Description **3**

2.1 General 3

2.2 The Octopole Ion Beam Guide 4

2.3 Kinetic Energy Scale and Doppler Broadening 5

2.4 Ion Sources 6

3 Theoretical Considerations **7**

4 Results **12**

4.1 Carbon, Oxygen and Silicon 12

4.2 Metals 16

4.3 Rare Gases 20

5 Analytic representation **23**

6 Discussion **25**

1 Introduction

The edge plasma in a tokamac nuclear fusion reactor is characterized by low plasma temperatures and high plasma densities. In the divertor region, the plasma temperature may be as low as a few eV, and plasma densities may be as high as $10^{17} cm^{-3}$.[1] An important consequence of the low edge plasma temperature is that molecular species are present in this region, resulting either from plasma-wall interactions (e.g. hydrocarbons) or from recycling and plasma fueling (molecular hydrogen and its isotopes). In addition to the primary constituents of the plasma, e.g. D, T and He (in DT plasmas) and H, D, and He in the present tokamaks, a relatively large variety (with concentrations between 0.1 and 10%) of atomic impurities are present. The most common impurity generating processes are particle-surface interaction processes, mainly desorption, physical sputtering and evaporation. The main impurities in the plasma edge of most of the present generation tokamaks and fusion reactor designs are carbon ($\leq$ 10%), oxygen ($\leq$ 5%), various metallic (and related) impurities originating from structural materials (Ti, V, Cr, Fe, Ni, Cu, Al, Mo, Mn, Mg, B, Si, Ge, Nb, Ag; with a concentration of $\leq$ 2%) and various diagnostic species (Li, Ne, Ar). Under these plasma conditions, a wide range of atomic and molecular processes that are not important in the core plasma become relevant.

Heavy particle interchange reactions in ion-molecule collisions refer to processes in which heavy particle rearrangment occurs, such as

$$A^{q+} + BC \rightarrow AB^{q+} + C. \tag{1}$$

In this report we will cover particle interchange reactions where the ion is a plasma impurity with a charge state q=1 and the molecule is either H_2, D_2 or HD. In general, there are two different types of these reactions. Endothermic reactions, which are characterized by a threshold below which the reaction does not take place (generally equivalent to the endothermicity of the reaction), and exothermic reactions, in which case the reaction often (but not always) occurs without an activation energy because of the attractive long-range interaction potential.[2],[3] Of the reactions presented here, all but the O^+, Ar^+ and Kr^+ systems are endothermic. The kinetic energy dependence of the interchange cross section for these two types of reactions is, of course, quite different. For exothermic reactions, the cross section often follows a relatively simple $E^{-1/2}$ decrease with increasing energy (in accord with the Langevin-Gioumousis-Stevenson prediction[4]), but deviations from this behavior abound.[5] For endothermic reactions, the cross section usually increases sharply starting at an energy close to the endothermicity of the reaction, peaks at an energy close to the molecular (H_2, D_2 or HD) dissociation limit, and decreases drastically within a few eV. The reason for this sharp decrease at high energies is that the dissociation channel opens, i.e. the reaction

$$A^+ + BC \rightarrow A^+ + B + C, \tag{2}$$

with a higher cross section, takes place. This decline in the interchange cross section after the dissociation energy has been reached may be delayed in energy if the reaction dynamics tends to place much of the excess energy in product translation.

2 Experimental Description

2.1 General

The work described in this report has been performed on a guided ion beam tandem mass spectrometer, that has undergone several changes in its 10 year history.[6]-[8] In this apparatus, ions exiting the ion source region are focused into a magnetic sector for mass analysis, decelerated to a desired kinetic energy, and injected into an octopole ion beam guide that passes through a collision cell filled with the neutral reactant. Pressures of this gas are generally kept sufficiently low that only single ion-molecule collisions are probable. (Deviations from single collision conditions are readily ascertained by examination of the pressure dependence of the product yield.) Product and reactant ions drift from the gas cell to the end of the octopole where they are extracted and focused into a quadrupole mass filter for mass analysis. The ions are then detected by using a secondary electron scintillation ion detector[9] and counted by using standard pulse counting electronics. A computer sweeps the kinetic energy of the ion beam while monitoring the reactant ion and all product ions so that extensive signal averaging can be performed easily.

Ion intensities are converted to absolute reaction cross sections as described previously.[6] Based on reproducibility, the relative uncertainty of cross sections at different energies is within about 5% for cross sections greater than $10^{-17} cm^2$ and is limited by statistical counting uncertainties for smaller cross sections. The absolute accuracy of the cross sections is limited by systematic errors in the measurement of

the absolute neutral reactant pressure and our estimate of the effective path length for interaction, both estimated at about 10%. Although the use of an octopole minimizes losses of ions, the possibility of ion loss especially at very low and very high energies cannot be ruled out entirely. For the heavy on light mass systems discussed in this work, collection deficiencies are minimized by the forward scattering in the laboratory frame necessitated by linear momentum conservation. Under most circumstances, we estimate that the uncertainties in the absolute cross sections are within ±20%. Comparison of the absolute cross sections measured with this instrument with calculated capture rate constants[10] and with thermal rate constant measurements[6],[11],[12] suggest that our cross sections generally suffer from no serious systematic errors and that their accuracy is very good.

2.2 The Octopole Ion Beam Guide

The octopole ion beam guide, first developed by Teloy and Gerlich,[13] is the primary key to the unique capabilities of this apparatus when compared with more conventional tandem mass spectrometers. A comprehensive analysis and description of such inhomogeneous rf devices has been made recently by Gerlich.[14] In our instrument, the octopole comprises eight rods (3.2 mm diameter) held in a cylindrical array (17.2 mm bolt circle). Alternate phases of an rf potential are applied to alternate rods such that an effective potential well in the radial direction is established. Energies along the axis of the octopole are perturbed little because the potential well, which depends on the inverse sixth power of the distance from the

center, is flat at the bottom and has steep sides.[6],[14],[15] One of the virtues of the octopole is that it enables the use of retarding field analysis to measure the absolute energy of the ion beam and its distribution. The octopole avoids problems associated with contact potentials, space charge effects and focusing aberrations because the analysis and interaction regions are physically the same. Further, the octopole trapping field prevents anomalous losses of ions even at very low kinetic energies. We have verified the ability of the octopole to accurately measure kinetic energies by comparison with time-of-flight experiments[6] and with calculated cross sections.[10] We estimate that the uncertainty associated with measuring the zero of energy is about 0.05 eV in the laboratory frame.

2.3 Kinetic Energy Scale and Doppler Broadening

Laboratory energies are converted to center-of-mass (CM) energies by using the stationary target assumption. Thus,

$$E_{CM} = E_{lab} \times m/(M+m), \tag{3}$$

where m and M are the masses of the neutral and ionic reactants, respectively. At the very lowest energies, this approximation is not adequate because the ion energy distribution is being truncated. In such circumstances, the mean energy that is reported properly reflects the truncated distribution of ions as described in detail previously.[6] This kinetic energy scale in the center-of-mass frame does not include the thermal motion of the reactant neutral, which adds another $(3/2)\gamma kT$ to the average energy where $\gamma = M/(M+m)$. These molecules have a Maxwell-

Boltzmann distribution of velocities at the temperature of the gas cell, usually T = 305 K in our work. The effects of this motion are to obscure sharp features in the true cross sections, a result that is especially obvious at a reaction threshold. In addition, the velocities of the neutral reactant molecules can be comparable to or larger than the ion velocities at very low kinetic energies. At these energies, the full distribution of neutral and ion velocities must be considered in order to fully describe the average interaction energy. The means necessary to describe this so-called Doppler broadening were first developed in detail by Chantry[16] for the cases of a monoenergetic ion beam and extended to include consideration of ion energy distributions by Lifshiftz et al.[17] The width of the energy distribution (fwhm) contributed by the neutral molecules at a center-of-mass energy, E, is given by Chantry as approximately $(11.1\gamma kTE)^{1/2}$.

2.4 Ion Sources

The guided ion beam apparatus shown in Figure 1 is capable of using several types of ion sources: commonly, surface ionization (SI), electron impact (EI) ionization, and two high pressure sources - a drift cell and a flow tube source. In some studies, several of these sources are used in order to systematically vary the degree of internal excitation of the ion. The SI source[18] can be used to ionize species with low ionization energies (IEs) such as metal atoms and is believed[19] to produce ions with a Maxwell-Boltzmann distribution of internal states at the temperature of the ionizing filament, 1900-2300 K. EI[18] can ionize and fragment any volatile gas,

but can produce internally excited species depending on the electron energy. The flow tube source, developed as a more versatile version of an earlier drift cell (DC) source,[20] is modeled after those of Lineberger[21] and Squires,[22] and is detailed in the literature.[8] This high pressure source ($\approx$ 0.5 Torr) is designed to produce atomic ions with a minimum of internal energy, that is, species thermalized to near room temperature.

3 Theoretical Considerations

The theoretical study of the particle-interchange reactions considered here is still an undeveloped field. It started about twenty years ago with the trajectory surface-hopping model first suggested by Bjerre and Nikitin[23] and the multivibronic curve crossing model introduced by Bauer, Fischer and Gilmore.[24] These two methods are based on the Landau-Zener model for the transition probability of a transition from one adiabatic curve to another. Quantum mechanical calculations are scarce, and mostly devoted to collinear systems or to three dimensions employing the infinite order sudden approximation.[25] Alternative simpler theories include statistical theories, such as phase space theory (PST) or transition state theory (TST), and empirical or semi-empirical approximations. Theoretical results for the reactions presented here are very scarce. In a few cases, PST results can be found in the literature.[26] Simons and coworkers have examined the B^+ and Al^+ targets by ab initio methods.[27]

The phase space theory for ion-molecule reactions[26],[28]-[30] uses the long range

ion-induced dipole potential (Langevin model) to determine the complex-formation cross section. These complex can then be decomposed into products or back to reactants via "loose" transition states.[26] Total energy and angular momentum are explicitly conserved. The presumption of loose transition states means that only the molecular parameters of isolated reactants and products are required to determine the number of states available in each channel. No explicit information regarding the complex or transition states is needed for PST calculations. In its simplest form, PST does not differentiate among any of the states in the reactant or product channels. All states which are accessible while conserving both energy and momentum are included in the statistical sum of states. Sums for electronic states which are degenerate are multiplied by the appropriate degeneracy factor.

It has been shown that classical phase space theory[31],[32] can be used instead of the full quantum mechanical version for the system for which PST calculations are presented here ($C^+ + H_2$). Details of the calculation can be found elsewhere.[26] The reaction cross section is given by:

$$\sigma(E) = (1/Q_{tot}) \sum_J (2J+1) g_i e^{-BJ(J+1)/kT} \sigma(E,J), \tag{4}$$

where Q_{tot} is the rotational partition function, B is the rotational constant, g_i is the nuclear spin degeneracy factor, T is the temperature of the target gas and $\sigma(E,J)$ is the cross section for a particular rotational state J of reactant hydrogen as a function of relative energy E given by[31]

$$\sigma(E,J) = \frac{\pi\hbar^2}{2\mu E} \frac{s}{2JG} \int_{K_-}^{K_+} dK \quad 2K N^{ots}_{reag}(E,J,K) \times N^{ots}_{prod}(E_0,K)/N^{ots}_{tot}(E_0,K), \tag{5}$$

where G and μ are the total number of degenerate electronic surfaces, and the reduced mass; s is the symmetry number; E and K are the relative translational energy of the reactants and the total angular momentum; E_0 is the total system energy defined as

$$E_0 = E + E_{rot} + E_{vib}; \tag{6}$$

$N^{ots}_{reag}(E, J, K)$ is the sum of orbital states of the reactants for given values of E, J and K; $N^{ots}_{prod}(E_0, K)$ is the total sum of states of the products for given values of E and K and $N^{ots}_{tot}(E_0, K)$ is the sum of the $N^{ots}_i(E_0, K)$ (total summ of states in channel i) over all available channels. Note that in all sums N all accessible electronic surfaces and reaction path degeneracy have been explicitly taken into account. Finally, K_- and K^+ are the maximum and minimum values of the total angular momentum K for which the reactive flux is greater than zero.

An important aspect of the reactions studied here are the isotopic effects, e.g. comparisons between the interchange cross sections for H_2, D_2 and HD. In particular, the branching ratio between reactions

$$A^+ + HD \rightarrow AH^+ + D \tag{7}$$

$$\rightarrow AD^+ + H \tag{8}$$

appears to be quite sensitive to reaction dynamics and is still not fully understood. For endothermic reactions, there seems to be three different types of behavior:[33] 1) the branching ratio is nearly unity; 2) the process in which AH^+ is formed is favored by a factor of about 3; and 3) the process in which AD^+ is formed is favored

by a large factor. In the first two types of reactivity, the reaction thresholds are observed to correspond to the thermodynamic thresholds, while in the third type, the experimental thresholds are higher than the thermodynamic thresholds and those for reactions 4 and 5 differ from each other and from those for reaction with H_2 and D_2.

The first type of isotopic behavior reflects approximately a statistically behaved system. This can be illustrated by examining the density of states for the products of the reactions given in Eq. 7 and 8. If we assume that the mass of A greatly exceeds the mass of H and D, a reasonable approximation for all cases studied here, the density of internal states favors the formation of AD^+. In the classical limit, the density of vibrational states is given by $1/\hbar\omega$, ω being the vibrational frequency. Because $\omega = (k/\mu)^{1/2}$ and the reduced mass $\mu(AH^+) \approx 1$ while $\mu(AD^+) \approx 2$, this favors the formation of AD^+ by a factor of $2^{1/2}$. The classical density of rotational states is $1/hcB$, where $B \propto 1/\mu$, hence the formation of AD^+ is favored by a factor of 2. The density of translational states is proportional to $m^{3/2}$, where m is the reduced mass of the reactant or product channel, $m(AD^+ + H) \approx 1$, while $m(AH^+ + D) \approx 2$. This gives an extra factor of $2^{3/2}$ in favor of AH^+. Overall, these factors approximately cancel such that the classical statistical isotope effect is about 1:1 formation of AH^+ and AD^+. This simple treatment ignores all quantum effects but does capture the essence of a statistically behaved system. More detailed calculations using PST give a branching ratio close to 1:1 for this cases.[26]

In the second type of systems, the formation of AH^+ is favored by a factor

which could be interpreted as a simple mass factor. In the analysis above, the internal density of states is the one favoring the formation of AD^+. If only the translational degrees of freedom are taken into account, the formation of AH^+ is favored by a factor of $2^{3/2} = 2.8$. This would reflect a direct reaction in which the internal degrees of freedom are unimportant.

The third type of behavior may be explained in a case where the energy relevant to a particle-interchange reaction is not the center-of-mass (CM) energy, but a "pairwise" interaction energy. In the CM frame, the energy available for chemical change is the relative kinetic energy between the incoming atom of mass M_A and the reactant molecule with mass $(M_B + M_C)$. The center of mass energy is given by Eq. (3) with $m = M_B + M_C$ and $M = M_A$. In a pairwise interaction, A is sensitive only to the potential between A and the interchanged atom B. Therefore, the pairwise energy for transfer of B from molecule BC is:

$$E_{B,BC} = E_{lab}\frac{M_B}{M_A + M_B}. \tag{9}$$

In cases where $M_A \gg M_B$ or M_C, substitution of Eq. (3) into Eq. (9) leads to the approximate relation:

$$E_{B,BC} = E_{CM}\frac{M_B}{M_B + M_C}, \tag{10}$$

such that the energy available for chemical change in a pairwise reaction is always less than E_{CM}. For reactions with BC=H_2 or D_2, this pairwise mass factor $\delta = M_B/(M_B + M_C)$ is 1/2. If BC=HD, then $\delta = 1/3$ if the transferred atom is H, while if the transferred atom is D then $\delta = 2/3$. This means that if the thermodynamic

threshold occurs at E_0, the pairwise threshold will occur at E_0/δ. Therefore, the enhanced production of AD^+ may be due to the lower apparent threshold for this reaction, $1.5E_0$, as compared to the one in which AH^+ is formed, $3E_0$. This pairwise scheme also explains the shift in the thresholds observed for the H_2 $(2E_0)$, D_2 $(2E_0)$, and HD systems.

4 Results

4.1 Carbon, Oxygen and Silicon

In many presently operating fusion devices carbon is one of the main impurities in a fusion plasma, reaching concentrations of up to 10%. Its presence in the plasma comes from the preferred use of graphite as plasma facing material, from first wall carbonization and from carbon contained in first wall alloys. The reaction

$$C^+(^2P) + H_2[D_2, HD] \rightarrow CH^+[CD^+] + H[D] \tag{11}$$

is probably the best studied endothermic reaction. The endothermicity of 0.398 ± 0.003 eV is known extremely well from spectroscopic data.[20]

The cross sections for reactions (11) are shown in Figure 2.[20] The reactions are clearly endothermic, with an extended plateau followed by a decline beginning at the dissociation energy of $H_2[D_2, HD]$. The apparent threshold is lower than the endothermicity, as shown more clearly in Figure 3. This is a consequence of the thermal motion of the $H_2[D_2, HD]$ reactant gas, as has been demonstrated elsewhere[34] and is illustrated by comparison with experimental results of Gerlich,

et al.[35] where a crossed beam of H_2 was used to drastically reduce this thermal motion. This broadening is a feature that is common to all the endothermic reactions discussed here. The reaction with D_2 has a cross section about two-thirds of that with H_2. In reaction with HD, formation of CD^+ is favored over that of CH^+ by a factor of about 1.4 from threshold until the onset of product dissociation, indicating type 1, statistical behavior. In part, CD^+ is favored slightly because this channel has a lower zero point energy and therefore a lower threshold by 45 meV.

Phase space theory calculations for this reaction agree well (within 15%) with experimental results.[26],[35] The input parameters to the PST calculation include the molecular parameters from reactants and products, all of which are well established, and the electronic degeneracies of the reactants and products. The agreement between PST and the experimental results shown in Figure 3 is obtained only when 1/3 of the reactant $C^+ + H_2$ surfaces are presumed to lead to products. This factor may be easily explained by molecular orbital analysis.[26] PST or any other theory is not able to fully explain the branching ratio observed in the HD reaction, indicating that dynamics play an important role in this reaction.

Oxygen is a common impurity in the plasma, reaching concentrations of up to 5%, basically because of its chemical activity and omnipresence, initially in the form of adsorbed H_2O films and after activation in the form of other oxygen containing compounds. One of the difficulties of examining the reactions of atomic oxygen ions is that excited electronic states are easily produced. The experimental results presented in Figure 4 were obtained with O^+ generated in an EI/DC source.[10] Ions

are first generated by electron impact ionization and fragmentation of CO_2, and then are passed through a drift cell filled with molecular nitrogen. Excited states of O^+ rapidly react with N_2 by charge transfer, while the ground state $O^+(^4S)$ ions react very slowly. The O^+ emerging from the cell is found to have less than 0.1% of excited states. The reaction

$$O^+(^4S) + H_2[D_2, HD] \rightarrow OH^+[OD^+] + H[D] \tag{12}$$

is exothermic by 0.6 eV.[36]

The cross sections for reactions (9) are shown in Figure 4.[10] They show three distinct energy regimes. At the lower energies, $\approx$ 0.25 eV, the cross section decreases as $E^{-1/2}$ as predicted by the Langevin-Gioumousis-Stevenson (LGS) collision model.[4] At energies above about 0.3 eV, the cross sections deviate from the LGS prediction such that the reaction efficiency drops. In the region between 0.3 and 5 eV, the cross sections fall approximately as E^{-1}. This behavior has been explained[10],[33] in terms of angular momentum conservation, because the reactants are higher in energy than the products but have a larger reduced mass than the products. This shifts the limiting transition state for reaction from the entrance channel at low energies to the exit channel at higher energies. Another effect may involve the lifetime of the ion-induced dipole bound $O^+ - H_2$ complex formed during the reaction. At low kinetic energies, the $O^+(^4S) + H_2$ system has time to orient into the collinear configuration favored by electronic considerations, while at higher kinetic energies, the time available to orient decreases (or equivalently the lifetime of the $O^+ - H_2$ complex decreases) such that the reaction efficiency falls off. At still

higher energies (above 5 eV), the cross sections drop more rapidly. This is due to the dissociation of the product ion in reaction 12, although dissociation to $O + H^+$ can also occur. The thermodynamic threshold for both dissociations is 4.5 eV. The observed onset of the decline in the OH^+ cross section is somewhat higher, about 6 eV, suggesting that some of the energy available to the products is preferentiably placed in translation. Flesch and Ng[37] find that the H^+ product appears at its thermodynamic threshold, but this could occur by a dissociative charge transfer process. The HD and D_2 system cross sections show the same energy behavior and comparable magnitudes as those of the H_2 system.

Silicon is a relatively important impurity in the plasma, frequently with a concentration of the order of a few percent. The main source of Si impurity atoms is from erosion of silicon additives. The reaction

$$Si^+(^2P) + H_2[D_2, HD] \rightarrow SiH^+[SiD^+] + H[D] \tag{13}$$

has an endothermicity of 1.26 $\pm$ 0.03 eV. Figure 5 shows the cross sections corresponding to reaction 10.[33],[38] In contrast with C^+ and O^+, the reaction with D_2 has a greater cross section than with H_2 (although they are within experimental error of one another), but with similar energy behavior. The plateau present in C^+ becomes a sharper peak because the reaction threshold is higher for Si^+. The position of the peak correlates with the dissociation threshold of $H_2[D_2]$. The reaction with HD is of type 1, based on the branching ratio in the threshold region. At higher energies, the formation of SiH^+ is favored over SiD^+ formation, an observation that was also true for the C^+ and O^+ systems and almost all cases presented here. This

simply is an indication that the D atom product carries away more energy than the H atom product, a result of it being more massive.

4.2 Metals

The presence of metallic impurities in the plasma edge is due mainly to erosion of structural materials. The expected relative abundance of these impurities in a fusion reactor is of the order of 1-2% for Al, Ti, Cr, Fe, Ni, Cu, B and V and less than 0.1% for the others. The reactions of H_2 $[D_2, HD]$ with the cations of these elements are all endothermic, with endothermicities of the order of a few eV. A common feature of metal ions that makes measurements of these reactions difficult is the large number of electronic states. For instance, V^+ has eight electronic states below 2 eV (28 spin-orbit levels)[39] which form 186 separate potential energy surfaces in the interaction with H_2. Clearly, explicit account of all these surfaces is quite difficult.

Because of the multitude of electronic states, the way the metal ions are produced has a very important influence on the results reported here. As noted in Section 2.4, there are three main ion sources used in these studies, surface ionization, electron impact and high pressure sources. In many cases, there exist cross section data for metal ions produced with different ion sources. Here, we present mainly those obtained by surface ionization, based on the fact that SI normally produce a high population of ions in the ground state, as compared to EI, for example.

Figure 6 shows the cross sections for the reaction

$$M^+ + H_2[D_2, HD] \rightarrow MH^+[MD^+] + H[D] \tag{14}$$

for $M = Al$.[40),(41)] Notice that all reactions are very inefficient, with cross sections not exceeding $10^{-18} cm^2$. The reaction with H_2 is more efficient than the one with D_2. The reactions have a large threshold that varies for all four reactions and that is higher than the thermodynamic threshold of 3.8 eV in all four cases. This energetic behavior and the branching ratios for the HD reaction indicate that this system has isotopic behavior that is largely type 3. In the HD system, AlH^+ formation is favored by a very large factor except at the lower energies, because AlD^+ formation has a lower energy threshold and maximum. An interesting dynamical explanation for this behavior has been forwarded by Simons and coworkers.[26]

Figures 7 and 8 show the cross sections for reaction (11) with $M = Ti$[42] and $M = V$,[18] respectively. The cross sections for the reactions with H_2 are bigger than with D_2, but still within experimental error. In the HD systems, formation of MH^+ and MD^+ have about the same cross section magnitudes in the threshold regions. All four reactions for both metals have similar thresholds. This indicates that these systems behave statistically (isotopic behavior type 1). At high energies in the HD reactions, the cross sections for MD^+ drop much faster than for MH^+, for reasons described above.

Figure 9 shows the cross sections for reaction (11) with $M = B$.[40),(41)] Results for B^+ are rather atypical and resemble those for Al^+. The cross section for H_2 is almost a factor of two larger than that for D_2, and the HD reaction has a mixed isotopic behavior, with formation of BH^+ favored at most energies but BD^+ favored at low energies. In both this and the analogous $Al^+ + HD$ system, the thresholds

are displaced from each other and from the thresholds of the H_2 and D_2 systems. Also the peaks in the various product cross sections are displaced from one another by several eV, and do not correspond to the dissociation energy for H_2, D_2, or HD. Also shown in Figure 9 are results of Ruatta, *et al.*[43] (open squares) divided by 2.75. The reason for this factor is not understood.

Figure 10 shows the cross sections for reaction (10) with $M = Cr$.[44] For this system, the reaction with H_2 is almost identical to the reaction with D_2, while the HD reaction has a mixed isotopic behavior most characteristic of type 3 because formation of CrD^+ is favored over formation of CrH^+. This mixed dynamic behavior accounts for the unusual double-peak structure in the latter cross section. Data appropriate for excited state Cr^+ generated by EI are also available in the literature.[44]

Figure 11 shows the cross sections for reaction (11) with $M^+ = Fe^+(^6D)$[45] and $Fe^+(^4F)$[45] for D_2 and HD. Notice that in this case the reactivity of the gorund state ($Fe^+(^6D)$) is much lower than the reactivity of an excited state ($Fe^+(^4F)$). The HD reaction in both cases is of type 2, formation of FeH^+ being favored by a factor of about 2.5.

Figures 12 and 13 show the cross sections for reaction (11) with $M = Ni$ and $M = Cu$.[46] In both cases, the H_2 and D_2 reactions are similar to one another, within experimental error, and the HD reaction is of type 2, formation of MH^+ favored by a relatively large factor (5 in the case of Ni^+ and almost 7 in the case of Cu^+ in the threshold region). All reactions rise from their thermodynamic thresholds

and reach maxima corresponding to the H_2, D_2, or HD bond energy (although the peaks in the MD^+ cross sections in the HD systems are somewhat lower because of competition with the MH^+ cross sections). Figure 14 corresponds to $M = Mo$.[47] In this case, the H_2 and D_2 are very similar and the HD reaction almost behaves statistically, type 1 behavior.

Figure 15 nad 16 show data for reaction of D_2 and HD with Mn^+ generated by SI and EI.[49] The SI source produces 99.83% of the ions in their ^{7}S ground state and 0.15% in the ^{5}S first excited state. The behavior of the D_2 cross section is very unusual. The cross section actually rises at an energy below the thermodynamic threshold for reaction of the ^{7}S state of $\approx$ 2.5 eV, indicating an observable contribution from the excited state. The reactivity of the ground state does not become appreciable until 5 eV, and the peak of the cross section is at an energy much higher than the thermodynamic onset of the dissociation channel, reaction 2. In fact, both the apparent threshold and the peak of the product ions are at energies approximately twice the thermodynamic values, in agreement with the predictions for type 3 behavior given in Section III. This is confirmed by the behavior of the HD data which shows a large preference for formation of MnD^+ and a shift in the threshold and peak of the cross section from the D_2 system. Figure 16 also shows results for reaction of D_2 and HD with Mn^+ in excited states,[49] obtained by EI ionization of $Mn_2(CO)_{10}$ at 50 eV electron energy. It is believed that the Mn^+ produced under these conditions has a population of about 50state, and the remainder in other uncharacterized states. The excited states are much more reactive than the

ground state of Mn^+, as is obvious from comparison of the D_2 results for the two source conditions. In contrast to the behavior of $Mn^+(7S)$, the excited Mn^+ behaves more like most of the transition metal ions presented here. The HD reaction is of type 2, with formation of MnH^+ being favored by a factor of about 3. Notice the double peak structure of the MnD^+ channel. This clearly shows the presence of both ground and excited state Mn^+ ions.

Figures 17-20 show data for reaction of H_2, D_2 and HD with Ag^+, Ge^+, Mg^+ and Zn^+. The concentration of these metallic ions in a fusion plasma is less than 0.1%.

4.3 Rare Gases

Rare gases are present in the plasma mainly due to their use for plasma diagnostics. Their concentration may reach up to a few percent. Rare gas ions (Rg^+) have the valence electron configuration $(ns)^2(np)^5$. Therefore the ground state are ^2P, like C^+ and Si^+. However, the reactivity of the ^2P states of Rg^+ are quite different from that of carbon and silicon ions. In the reactions of O^+, C^+, and Si^+ with H_2, the reactants in the particle interchange process readily reach the products on a single adiabatic potential energy surface in the entrance channel.[59] For the Rg^+, there is a second important surface in the entrance channel, namely the charge transfer channel $Rg + H_2^+$. Mahan[58] has pointed out that the $RgH^+ + H$ products correlate with $Rg + H_2^+$ and not with $Rg^+ + H_2$. This is demostrated by the observation that the endothermic reaction $He + H_2^+ \rightarrow HeH^+ + H$ is efficient and easily driven by

traslational and vibrational energy.[60] The coupling between these two entrance channel surfaces depends strongly on their relative energies as determined by the relative ionization potentials of H_2 and the rare gases. Therefore, the effects of this coupling vary substantially among different rare gases.

The reaction

$$Rg^+ + H_2[D_2, HD] \rightarrow RgH^+ + H \tag{15}$$

for $Rg = Ne$ is exothermic by 5.6 eV. Yet this reaction show no reactivity until the relatively high energy of 9.8 eV,[26] as shown in Fig. 21. The basic reason for this non-reactivity is the fact that the reaction Ne^+ with H_2 occurs on a surface which lies well above that corresponding to $Ne + H_2^+$, and this surface correlates with the desired products, $NeH^+ + H$.[58],[61],[62] Further insight into this reaction may be obtained from the work of Jones *et al.*,[62] who studied the $He^+(^2S)$ reaction and examined the luminiscence from this reaction. Since reaction 15 with $Rg = He$ shows a similar behaviour as the one with $Rg = Ne$, their conclusion may be extended to Ne.[26] Extensive Balmer and Lyman emision was observed with an onset for Lyman α emission coincident with the onset for HeH^+ formation. Thus the process being observed is

$$Rg^+(^2X) + H_2(^1\Sigma_g^+) \rightarrow RgH^+(^1\Sigma) + H^*(2p). \tag{16}$$

Since $H(2p)$ is 10.2 eV above the H(1s) ground state, reaction 16 is endothermic by 1.9 eV for $He^+(^2S)$ and by 4.6 eV for $Ne^+(^2P)$. While this can explain the endothermicity of reaction 15, the observed threshold of $\approx$ 10 eV is well above

the calculated endothermicity. Furthermore, the peak in the cross section is also displaced to $\approx$ 18 eV. Examination of this reaction with D_2 and HD helps explain this behaviour. The cross section for reaction 15 with D_2 is identical in shape but vary somewhat in magnitude compared to the H_2 reaction cross section. The threshold for this reaction is twice the thermodynamical threshold of 4.6 eV (9.2 eV in the CM frame). For reaction with HD to form NeH^+, the pairwise threshold is 13.8 eV (3×4.6) and to form NeD^+ it is 6.9 eV (1.5×4.6). While the agreement with the data is not quantitative, these energies are in rough agreement with the observed thresholds.

The cross sections for reaction (15) with $Rg = Ar$ are shown in Fig. 22. This reaction has been considered as a classic example of an exothermic reaction which porceeded at the LGS collision limit. It has been shown[6] that the cross section, as shown in Fig. 22, deviates from the LGS for both D_2 and H_2. The total cross section for HD is also comparable, except in the region where dissociation of the product becomes important, $>$ 4 eV. At the lowest energies, reaction (15) occurs with a reaction efficiency of two-thirds, in agreement with several rate constant measurements[64][65],[66] This disagrees with the conclusion of a simple MO treatment that only one-third of the surfaces should be reactive. This disagreement may be explanined by the fact that spin-orbit effects play an important role (see for example Refs.,[67][68]), since a reaction efficiency of two-thirds is expected in beam with a statistical mixture of $^2P_{3/2}$ and $^2P_{1/2}$ states. Fig. 23 shows spin-orbit-state dependence of the cross section for the reaction $Ar^+ + H_2 \rightarrow ArH^+ + H$. As the

kinetic energy increases, the reaction efficiency increases to about 90% near 1 eV. Above this energy, the cross section drops as E^{-1} until about 4 eV, where it falls off rapidly. The branching ration between ArH^+ and ArD^+ is nearly unity until dissociation.

The cross sections for reaction (15) with $Rg = Kr(^2P_{3/2})$ are shown in Fig. 24.[69] This reaction is exothermic by 0.29±0.06 eV, while the $^2P_{1/2}$ state reaction also shown in Fig. 25 is exothermic by 0.96 eV. Notice that the spin orbit dependence of the reaction is very strong. The cross section for the $^2P_{3/2}$ state shows a feature at high energies which is not found for the $^2P_{1/2}$ state. The total cross sections of Fig. 24 show an unusual intermolecular isototpe effect such that the relative magnitudes are $\sigma(HD) > \sigma(H_2) > \sigma(D_2)$. Some of these features may be explained by examination of the diabatic and adiabatic surface correlations (see Ref.[59]

5 Analytic representation

In many applications, plasma modeling for example, cross sections or rate coefficients of different processes are required over a wide energy region. Analytic fits to the data serve this purpose, because with few parameters and a given function, the cross sections can be generated easily. Compared to polynomial fits, non-linear analytic fits do not have spurious oscillations and can represent the low and high energy limits properly.

In this work, we have made analytic fits to all data presented. The functions used are (E refers to center of mass energy in eV):

Expression 1:

$$\sigma = a_1 \exp\left[\frac{-(E-a_2)^2}{a_3}\right] E^{a^4} + a_5 \exp\left(-a_6 E\right) E^{a_7} \tag{17}$$

Expression 2:

$$\sigma = a_1 \frac{\exp\left(-a_2/E^{a_3}\right)}{1 + a_4 E^{a_5}} + a_6 \exp\left(\frac{-a_7}{E^2}\right) E^{a_8} \tag{18}$$

Expression 3:

$$\sigma = a_1 \frac{\exp\left(-a_2/E^{a_3}\right)}{1 + a_4 E^{a_5}} + a_6 \exp\left(\frac{-a_7}{E^{1.5}}\right) E^{a_8} \tag{19}$$

Expression 4:

$$\sigma = a_1 \exp\left[\frac{-(E-a_2)^2}{a_3}\right] (1 + a_4 E^{a_5}) \tag{20}$$

Expression 5:

$$\sigma = a_1 \exp\left(-a_2 E\right)(E^{a_3} + a_4 E^{a_5}) + a_6 \exp\left(-a_7 E\right) \tag{21}$$

Expression 6:

$$\sigma = a_1 \exp\left(-a_2 E\right) E^{a_3} + a_4 E^{a_5} \exp\left(-a_6/E\right) \tag{22}$$

Expression 7:

$$\sigma = \frac{a_1 ln(a_2 E^{-a3} + a_4)}{1 + a_5 E^{a_6}} + a_7 \exp -a_8 E^{a_9} \tag{23}$$

Table 1 gives the expression used to represent the cross sections for each reaction and the corresponding parameters in equations 15 - 20.

In using these analytic fits to model systems, it should be remembered that the experimental conditions for the system being modeled may differ from the experimental conditions used to generate these data. The kinetic energy distributions of the ions and neutrals and the electronic states of the ions influence the shapes of these cross sections. Reactions taking place at higher neutral reactant densities may also lead to different reaction channels than those shown here, which correspond to single collision conditions in all cases.

6 Discussion

We have seen that many endothermic particle interchange reactions between metallic ions and H_2 (or D_2) follow a pattern: the cross section rises from an apparent threshold, peaks at an energy close to the dissociation energy of the neutral reactant, and then decreases relatively rapidly. This regularity can be seen clearly in Figure 26, where we show the cross sections σ/σ_0 as a function of scaled energy E/E_0, where σ_0 and E_0 are the values of the cross section and the energy at the peak. For most of these reactions, E_0 is close to the bond energy of D_2, while for $M = Al, B, Mg, Mn$, and Zn the value is displaced to higher energies.

The similarities between these various curves reflect the similarity in the overall physical processes. In the case of transition metal ions, a more detailed comparison can be found elsewhere.[70] The apparent symmetry above and below the peak for each particular system is largely serendipitous because the molecular characteristics that control the onset of reaction (formation of $MD^+ + D$) are not the same as

those that control the decline (dissociation to $M^+ + 2D$). This is evident from the data for M = C, shown in Figure 2, that does not exhibit this type of symmetry. Some correlation between how rapidly the cross section rises from threshold and how fast it declines above its maximum is observed because the threshold for reaction is lowest when the MD^+ bond is strongest, and this also means that the MD^+ product is less likely to dissociate at higher energies.

Although not presented here in detailed form, the interested reader can also find kinetic energy dependent cross sections in the literature for reaction of H_2, D_2, and HD with other rare gas ions (He^+,[53] Xe^+[55]), other atomic metal ions (Ag^+,[50] Mg^+,[51] Zn^+,[52] Ca^+,[52] Sr^+,[51] Sc^+, Y^+, La^+, and Lu^+[56]), other atomic ions (H^+, D^+,[14] N^+[57],[71] and S^+[72]), and several molecular ions O_2^+,[73] N_2^+,[74] N_4^+,[75] H_2^+,[76] H_3^+, and D_3^+[14]).

Acknowledgments

The experimental data presented here was acquired with support of the National Science Foundation. C.I. and J. B. would like to thank Prof. R.K. Janev for helpful discussions.

References

1. R.K. Janev, M.F.A. Harrison, H.W. Drawin, Nuclear Fusion 29, 109 (1989).

2. V.L. Talrose, P.S. Vinogradov, I.K. Larin, in Gas Phase Ion Chemistry, Vol. 1; Ed. M. Bowers; Academic: New York, p. 305 (1979).

3. P.B. Armentrout, in Advances in Gas Phase Ion Chemistry, Vol. 1; Eds. N.G. Adams, L.M. Babcock.; JAI: Greenwich, 83 (1992).

4. G. Gioumousis, D.P. Stevenson J. Chem. Phys. 29, 294 (1958).

5. P.B. Armentrout, in Structure/Reactivity and Thermochemistry of Ions, P. Ausloos, S. G. Lias, Eds.; D. Reidel, Dordrecht, 1987; pp. 97-164.

6. K.M. Ervin, P.B. Armentrout, J. Chem. Phys. 83, 166 (1985).

7. L.S. Sunderlin, P.B. Armentrout, Chem. Phys. Lett. 167, 188 (1990).

8. R.H. Schultz, P.B. Armentrout, Int. J. Mass Spectrom. Ion Processes, 107, 29 (1991).

9. N.R. Daly, Rev. Sci. Instrum. 31, 264 (1959).

10. J.D. Burley, K.M. Ervin, P.B. Armentrout, Int. J. Mass Spectrom. Ion Processes 80, 153 (1987).

11. J.D. Burley, P.B. Armentrout, Int. J. Mass Spectrom. Ion Processes 84, 157 (1988).

12. E.R. Fisher, P.B. Armentrout, J. Chem. Phys. 94, 1150 (1991).

13. E. Teloy, D. Gerlich, Chem. Phys. 4, 417 (1974); D. Gerlich Diplomarbeit, University of Freiburg, Federal Republic of Germany (1971).

14. D. Gerlich, Adv. Chem. Phys. 82, 1 (1992).

15. K.M. Ervin, Ph.D. Thesis, University of California, Berkeley, 1986.

16. P.J. Chantry, J. Chem. Phys. 55, 2746 (1971).

17. C. Lifshitz, R.L.C. Wu, T.O. Tiernan, D.T. Terwilliger, J. Chem. Phys. 68, 247 (1978)

18. J.L. Elkind, P.B. Armentrout, J. Phys. Chem. 89, 5626 (1985).

19. L.S. Sunderlin, P.B. Armentrout, J. Phys. Chem. 92, 1209 (1988).

20. K.M. Ervin, P.B. Armentrout J. Chem. Phys. 84, 6738 (1986).

21. D.G. Leopold, K.K. Murray, A.E.S. Miller, W.C. Lineberger, J. Chem. Phys. 83, 4849 (1985).

22. S.T. Graul, R.R. Squires, Mass Spec. Rev. 7, 263 (1988).

23. A. Bjerre, E.E. Nikitin, Chem. Phys. Lett. 1, 179 (1967).

24. E. Bauer, E.R. Fischer, F.R. Gilmore, J. Chem. Phys. 51, 4173 (1969); M.S. Child, M. Baer, J. Chem. Phys. 74, 2832 (1981).

25. M. Baer, Adv. Chem. Phys. 82 Part II, 202; M. Baer, C. Y. Ng, D. Neuhauser, Chem. Phys. Lett. 93, 4845 (1990).

26. K.M. Ervin, P.B. Armentrout, J. Chem. Phys. 84, 6750 (1986).

27. M. Gutowski, M. Roberson, J. Rusho, J. Nichols, J. Simons, J. Chem. Phys. 99, 2601 (1993).

28. C.D. Light, J. Chem. Phys. 40, 3221 (1964); P. Pechukas and J.C. Light, J. Chem. Phys. 42, 3281 (1965).

29. E.E. Nikitin, Teor. Eksp. Khim. 1, 135, 144, 248 (1965) [Theor. Exp. Chem. (end. Trans. 1, 83, 90, 275 (1975)].

30. J.. Light, J. Chem. Phys. 43, 3209 (1965).

31. D.A. Webb, W.J. Chesnavich, J. Phys. Chem. 87, 3791 (1983).

32. W.J. Chesnavich, M.T. Bowers, J. Chem. Phys. 66, 2306 (1977)

33. P.B. Armentrout, in Isotope Effects in Chemical Reactions and Photodissociation Processes, J.A. Kaye, Ed.; ACS Symp. Ser. 502, 194 (1992).

34. L.S. Sunderlin, P.B. Armentrout, J. Chem. Phys. 100, 5639 (1994).

35. D. Gerlich, R.Disch, S. Scherbarth, J. Chem. Phys. 87, 350 (1987).

36. D.D Wagman, W.H. Evans, V.B. Parker, R.H. Schumm, I. Halow, S.M. Bailey, K.L. Churney, R.L. Nuttall, J. Phys. Chem. Ref. Data 11, Supp. 2 (1982).

37. G.D. Flesch, C.Y. Ng, J Chem. Phys. 94, 2372 (1991).

38. J. L. Elkind, P. B. Armentrout, J. Phys. Chem. 88, 5454 (1984).

39. J. Sugar, C. Corliss, J. Phys. Chem. Ref. Data 14, Suppl. 2 (1985).

40. P.B. Armentrout, Int. Rev. Phys. Chem. 9, 115 (1990).

41. J.L. Elkind, P.B. Armentrout, unpublished data (1985).

42. J.L. Elkind, P. B. Armentrout, Int. J. Mass Spectrom. Ion Processes 83, 259 (1988).

43. S. Ruatta, L. Hanley, S.L. Anderson, J. Chem. Phys. 91, 226 (1989).

44. J.L. Elkind, P. B. Armentrout, J. Chem. Phys. 86, 1868 (1987).

45. J.L. Elkind, P.B. Armentrout, J. Phys. Chem. 90, 5736 (1986).

46. J.L. Elkind, P.B. Armentrout, J. Phys. Chem. 90, 6576 (1986).

47. J.L. Elkind, P.B. Armentrout, unpublished data (1986).

48. M. Sievers, P.B. Armentrout, work in progress.

49. J.L. Elkind, P.B. Armentrout, J. Chem. Phys. 84, 4862 (1986).

50. Y.-M. Chen, P.B. Armentrout, work in progress.

51. N.F. Dalleska, K.C. Crellin, P.B. Armentrout, J. Phys. Chem. 97, 3123 (1993).

52. R. Georgiadis, P.B. Armentrout, J. Phys. Chem. 92, 7060 (1988).

53. K.M. Ervin, P.B. Armentrout, J. Chem. Phys. 86, 6240 (1987).

54. K.M. Ervin, P.B. Armentrout, J. Chem. Phys. 85, 6380 (1986).

55. K.M. Ervin, P.B. Armentrout, J. Chem. Phys. 90, 118 (1989).

56. J.L. Elkind, L.S. Sunderlin, P.B. Armentrout, J. Phys. Chem. 93, 3151 (1989).

57. K.M. Ervin, P.B. Armentrout, J. Chem. Phys. 86, 2659 (1987). Ng, J. Chem. Phys. 84, 4317 (1986).

58. B.H. Mahan, J. Chem. Phys. 55, 1436 (1071); Accts. Cehm. Res. 8, 55 (1975).

59. P.B. Armentrout, Int. Rev. Phys. Chem. 9, 115 (1990).

60. W.A. Chupka, M.E. Russell, J. Chem. Phys. 49, 5426 (1968).

61. B.H. Mahan, J.S. Winn, J. Chem. Phys. 57, 4321 (1972).

62. P.J. Kuntz, A.C. Roach, J. Chem. Soc. Faraday Trans. II 68, 259 (1972).

63. E.G. Jones, R.L.C. Wu, B.M. Hughes, T.O Tiernan, D.G. Hopper, J. Chem. Phys. 73, 5631 (1980).

64. R.D. Smith, D.L. Smith, J.H. Futrell, Int. J. Mass Spectrom. Ion Phys. 19, 295 (1076).

65. I. Dotan, W. Lindinger, J. Chem. Phys. 76, 4972 (1982).

66. P.R. Ke,per, M.T. Bowers, Int. J. Mass Spectrom. Ion Phys. 52, 1 (1983).

67. K. Tanaka, J. Durup, T. Dato, I. Koyano, J. Chem. Phys. 74, 5561 (1981).

68. C-Y Ng, Advances in Chem. Phys. Series 82, 401 (1992).

69. K.M. Ervin, P.B. Armentrout, J. Chem. Phys. 85, 6380 (1986)

70. J.L. Elkind, P.B. Armentrout, J. Phys. Chem. 91, 2037 (1987).

71. P. Tosi, O. Dmitriev, D. Bassi, O. Wick, D. Gerlich, J. Chem. Phys. 100, 4300 (1994).

72. G.F. Stowe, R.H. Schultz, C.A. Wight, P.B. Armentrout, Int. J. Mass Spectrom. Ion Processes 100, 177 (1990).

73. M.E. Weber, N.F. Dalleska, B.L. Tjelta, E.R. Fisher, P.B. Armentrout, J. Chem. Phys. 98, 7855 (1993).

74. R.H. Schultz, P.B. Armentrout, J. Chem. Phys. 96, 1036 (1992).

75. R.H. Schultz, P.B. Armentrout, J. Chem. Phys. 96, 1046 (1992).

76. C.L. Liao, C.Y. Ng, J. Chem. Phys. 84, 197 (1986). J.D. Shao, C.Y.

Tabla 1: Parameters for the analytic fits.

Reaction	Fit *	a_1	a_2	a_3	a_4	a_5	a_6	a_7	a_8
$C^+ + H_2$	2	2.4227	0.5648	0.9831	0.1369E-03	4.6645	0.6892	0.4532	-1.8112
D_2	2	1.7700	0.9278	0.7499	0.7214E-04	5.2681	1.0260	0.4429	-1.3375
HD^1	3	1.2963	1.3037	0.5859	0.7382E-03	3.7451	0.9493	0.8375	-1.7938
HD^2	3	1.5651	0.8339	0.7394	0.1034E-04	6.4434	0.6915	0.7923	-1.9521
$O^+ + H_2$	5	6.0584	1.9028	-0.4232	2.2762	-0.4232	8.9380	0.2401	
D_2	5	21.0010	3.3203	-0.3685	1.7340	0.8621	7.6810	0.2333	
HD^1	5	0.4904	0.1755	0.4052	9.7028	-0.5835	13.7129	2.0795	
HD^2	5	1.9387	0.4342	1.1924	2.3245	-0.5638	8.3116	10.1516	
$Si^+ + H_2$	1	0.6876E-04	4.8919	1.2857	4.7086	0.5440	0.8670	3.2978	
D_2	1	0.5697	-6.9803	26.4962	4.1046	2.2621	3.5354	8.2685	
HD^1	1	1.6141	5.0946	1.6592	-1.5019	0.1650	1.2931	4.7125	
HD^2	1	1.5127	-6.6639	23.1747	3.3913	0.3123E-01	0.5350	3.2391	
$Ge^+ + H_2$	1	0.4174	-2.6944	2.1957	13.0924	0.7389E-01	1.4102	6.2168	
D_2	1	0.9565	-3.3142	3.3746	9.8594	0.6038E-01	1.5044	6.5809	
HD^1	1	1.8548	-6.4204	11.0892	5.9428	0.7186E-02	1.0455	6.1512	
HD^2	1	0.7723	-7.6205	12.8199	7.8544	23.2726	12.4083	28.0961	
$Ag^+ + H_2$	1	0.6568E-02	4.3669	0.5480	2.5636	0.2403E-11	8.2219	41.0891	
D_2	1	31.2781	5.2694	0.7968E-01	-20.3268	0.8077E-12	12.1637	54.2531	
HD^1	1	0.6241E-02	4.9196	0.8591	2.1010	0.2402E-10	5.1786	30.3243	
HD^2	6	0.1256E-12	11.4063	51.2384	0.2972	7.6263	-2.0464		

* Refers to the expressions given in Equations (17)-(23).

[1] $M^+ + HD \rightarrow MH^+ + D$

[2] $M^+ + HD \rightarrow MD^+ + H$

Tabla 1: Continuation.

Reaction	Fit *	a_1	a_2	a_3	a_4	a_5	a_6	a_7
$Al^+ + H_2$	1	0.3689E-03	8.8721	2.2142	1.3995	0.1324E-18	2.7312	28.2325
D_2	4	0.6743E-02	9.3068	2.0824	0.2082E-19	18.9947		
HD^1	4	0.1512E-05	9.5038	5.5735	3.5403	0.1341E-15	1.9512	22.1544
HD^2	1	1.2262	7.1585	1.7567	-3.1487	0.5927E-13	2.8017	22.4889
$B^+ + H_2$	1	0.4247E-03	-12.8882	30.1688	10.2213	16.3517	7.7797	7.6294
D_2	1	0.3757	7.7428	1.5123	-0.9222	0.2673E-05	1.4359	10.8769
HD^1	1	0.2990E-04	7.4047	1.7672	3.8732	0.1214E-05	1.0626	9.8244
HD^2	1	0.9230E-05	-2.1215	11.2994	8.5916	0.1615E-04	0.7957	6.3676
$Cr^+ + H_2$	1	0.7354E-05	2.6543	3.6829	6.5795	0.1816E-05	1.9784	12.3483
D_2	1	0.9763E-06	1.7888	4.0930	8.5821	0.5181E-06	1.8249	12.2406
HD^1	1	6.5527	4.5010	0.6620	-4.2398	0.2118E-06	1.7485	12.3046
HD^2	1	0.2120E-06	2.2394	2.4814	9.3736	0.5945E-05	1.4206	9.1519
$Cu^+ + H_2$	1	0.1670E-01	4.1239	0.5959	2.0283	0.3612E-09	8.0077	37.7967
D_2	1	0.1750E-02	4.1422	0.7491	3.9534	0.2205E-08	5.6379	28.8868
HD^1	1	0.1772E-03	4.1628	0.8936	4.7420	0.5790E-07	3.9176	22.0742
HD^2	1	32.5852	-8.9097	2.7951	38.6171	0.3700E-03	1.1177	5.3696
$Fe^+(^6D) + D_2$	1	5.6502	5.5811	0.7878E-04	0.7230E-01	0.4417E-04	1.3478	9.0108
HD^1	1	0.2051	-5.5536	6.4411	10.0888	0.2923E-02	1.4364	7.4147
HD^2	1	0.1091E-03	5.4707	2.8138	3.4492	0.7654E-02	1.1503	5.3401
$Fe^+(^4F) + D_2$	1	0.27360	4.67460	0.59530	0.63010	0.4540E-3	0.84440	6.0719
HD^1	1	0.1533	-4.1450	5.1848	10.348	0.14517E-01	1.5567	7.7585
HD^2	1	0.1484	-3.3170	3.6668	10.501	0.4155E-02	1.4992	6.9894

* Refers to the expressions given in Equations (17)-(23).

[1] $M^+ + HD \rightarrow MH^+ + D$

[2] $M^+ + HD \rightarrow MD^+ + H$

Tabla 1: Continuation.

Reaction	Fit *	a_1	a_2	a_3	a_4	a_5	a_6	a_7
$Mg^+ + H_2$	1	0.3424E-05	1.5051	14.9878	5.9390	0.8094E-02	2.2444	0.5252
D_2	1	0.9140E-05	4.5121	0.6696	3.4206	0.1210E-09	2.2676	18.1563
HD^1	1	0.1254E-02	4.2359	0.2873E-01	-0.1186	0.2146E-04	0.6322	4.7068
HD^2	1	0.4347E-06	1.0594	7.3930	8.4011	0.3013E-05	0.6466	5.8995
$Mn^+ + D_2$	1	0.3220E-05	6.6032	5.6048	5.0548	0.1650E-02	0.1785	1.2988
HD^1	1	122.6415	6.5709	0.9055E-01	-68.1373	0.7997E-03	0.8379	3.9994
HD^2	1	0.4830E-04	4.8650	3.6120	4.6836	0.3127E-06	1.6829	11.9207
$Mo^+ + H_2$	1	0.1816E-04	2.1826	1.5543	7.9769	0.4972E-04	3.2083	15.6359
D_2	1	0.1926E-04	-0.4929	4.0158	10.5236	0.3775E-04	2.5744	13.5932
HD^1	1	0.1800E-04	2.3841	2.1239	7.5721	0.1367E-04	2.1381	12.5991
HD^2	1	0.7533E-03	3.6189	1.8516	3.9266	0.5133E-05	2.4155	13.3818
$Nb^+ + H_2$	1	1.5223	-9.5323	25.3637	4.9966	-10.3680	7.1868	14.7585
D_2	1	0.6861	-8.4661	20.8691	5.6957	-8.1364	7.8389	16.6475
HD^1	1	115.8729	4.5951	0.8161E-02	-5.5772	0.6879E-02	2.4215	10.8280
HD^2	1	616.3727	4.9555	0.9216E-01	-40.8749	0.1256E-02	2.7818	12.0326
$Ni^+ + H_2$	1	0.3563E-03	3.0002	1.4252	6.1225	0.4069E-04	3.7812	17.7161
D_2	1	0.4115E-03	2.9791	1.7485	6.0246	0.3029E-04	2.5064	13.2607
HD^1	1	0.2360E-04	-1.1986	4.0207	12.0903	0.4559E-04	2.4243	13.3949
HD^2	1	0.2484E-03	2.5367	1.4873	5.8079	0.6917E-04	1.7151	9.1565

* Refers to the expressions given in Equations (17)-(23).

[1] $M^+ + HD \rightarrow MH^+ + D$

[2] $M^+ + HD \rightarrow MD^+ + H$

Tabla 1: Continuation.

Reaction	Fit *	a_1	a_2	a_3	a_4	a_5	a_6	a_7
$Ti^+ + H_2$	1	0.2583E-02	-4.7730	14.3468	7.2519	0.7673E-02	2.9512	10.8452
D_2	1	0.3020E-06	2.2869	0.5557	10.9316	0.2999E-02	1.7810	8.5950
HD^1	1	0.2015E-01	-6.2360	11.1255	7.8524	0.2843E-03	1.2340	7.5683
HD^2	1	0.4398E-02	4.1688	2.1959	2.0990	0.1370E-02	1.4925	7.0814
$V^+ + H_2$	1	0.4411E-03	-2.9449	3.4480	13.8489	0.7630E-03	2.0604	10.1866
D_2	1	0.2279E-02	-4.4457	5.4449	12.1460	0.6615E-03	1.6011	8.6188
HD^1	1	0.1402E-02	-4.2247	5.6416	11.3306	0.1432E-03	1.4533	8.6303
HD^2	1	0.5596E-03	3.3363	2.8820	4.0073	0.2565E-04	1.7036	9.7621
$Zn^+ + H_2$	1	0.2505	4.5991	0.1561E-03	-0.3726	0.2522E-05	1.6796	12.3514
D_2	1	0.4839E-01	4.6978	0.8887E-04	-0.4276	0.6046E-06	1.9485	14.1202

* Refers to the expressions given in Equations (17)-(23).

[1] $M^+ + HD \rightarrow MH^+ + D$

[2] $M^+ + HD \rightarrow MD^+ + H$

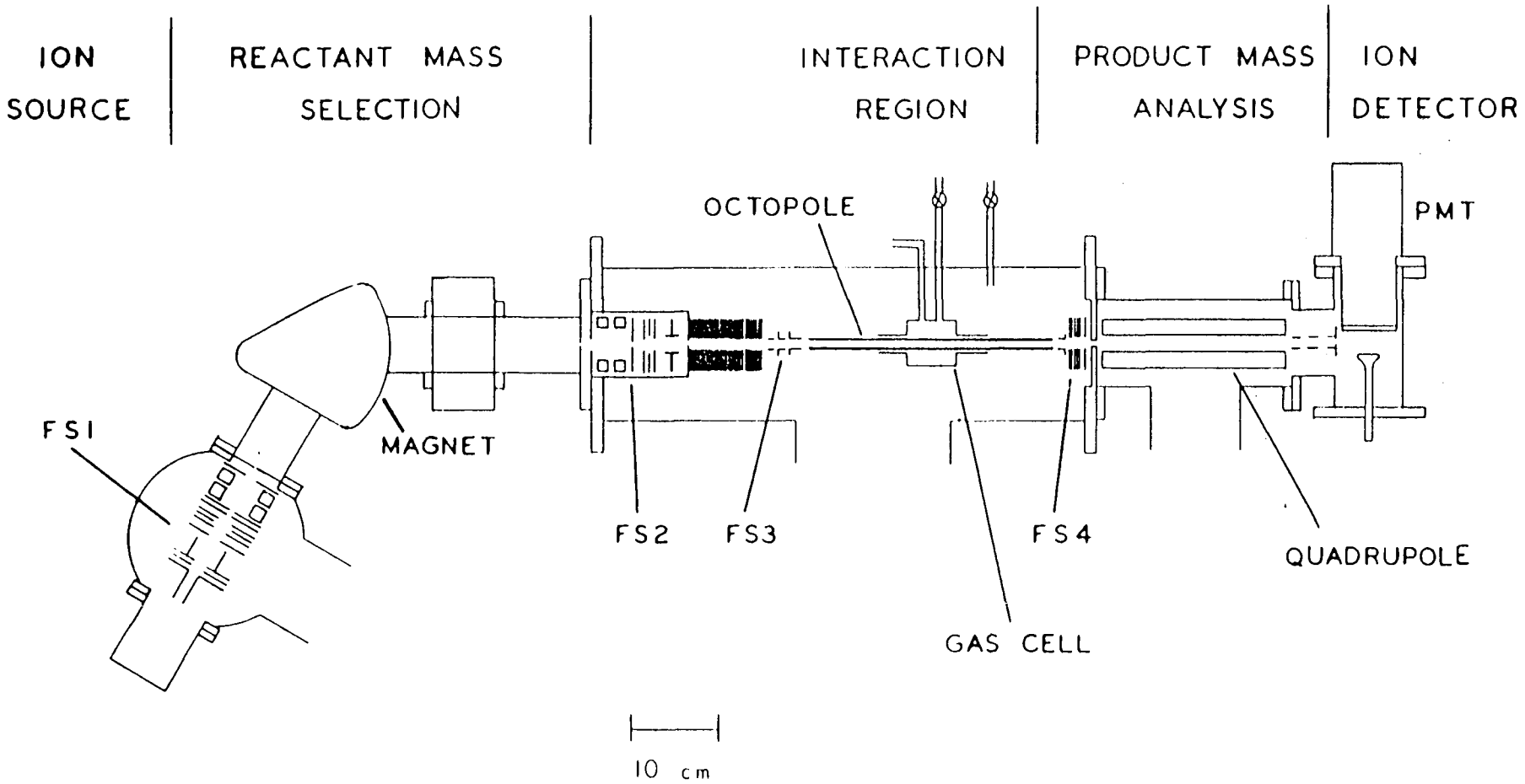

Figure 1: Schematic overview of the guided ion beam tandem mass spectrometer. (Reprinted with permission of VCH Publishers).

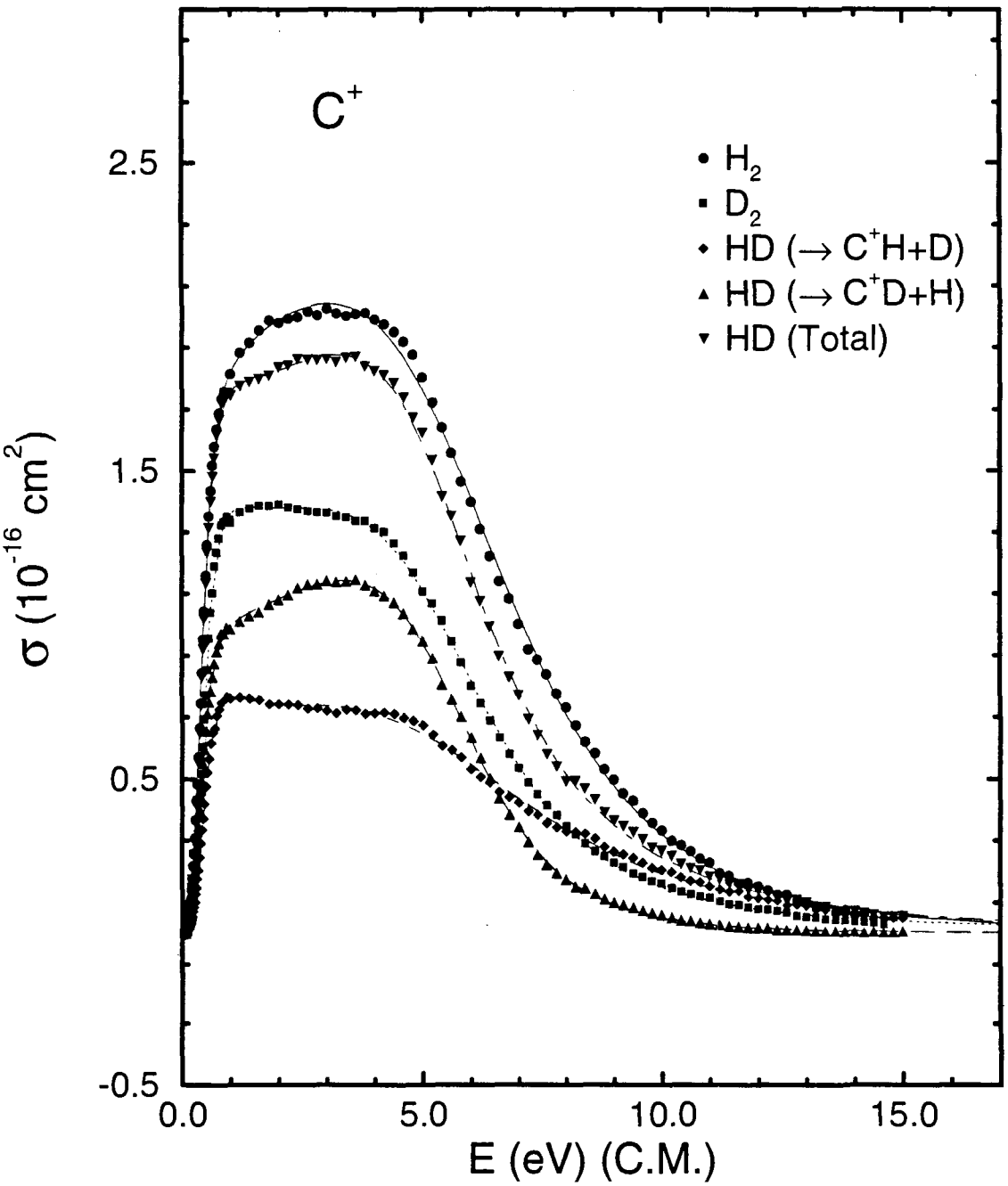

Figure 2: Cross sections for reaction of C^+ with H_2, D_2 and HD as a function of relative kinetic energy. The lines show the analytic fits with the coefficients given in Table 1.

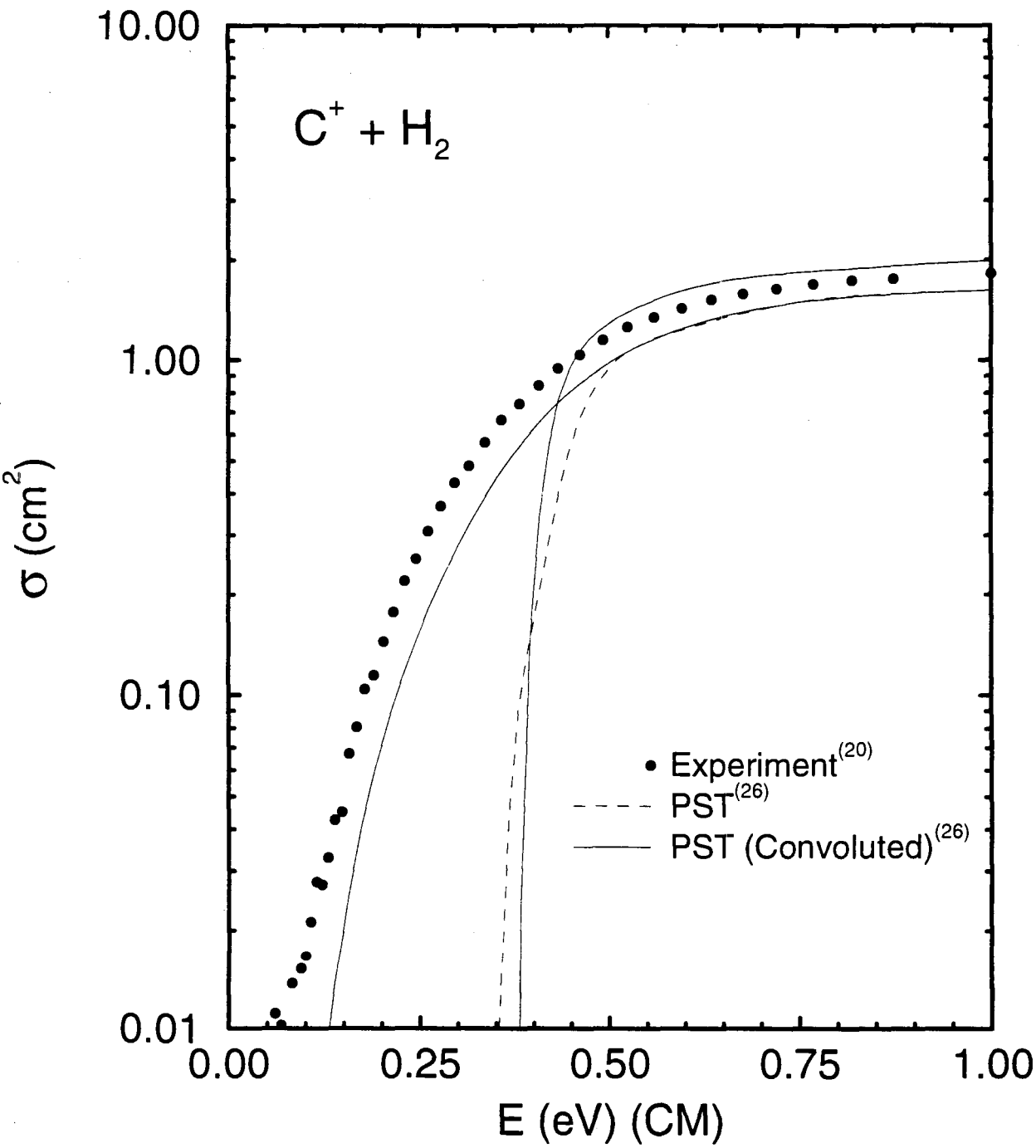

Figure 3: Cross sections for reaction of C^+ with H_2 at low relative kinetic energy. The dashed and dotted lines show phase space calculations for this process[26,35] The full lines gives the calculation convoluted with the experimental energy broadening.

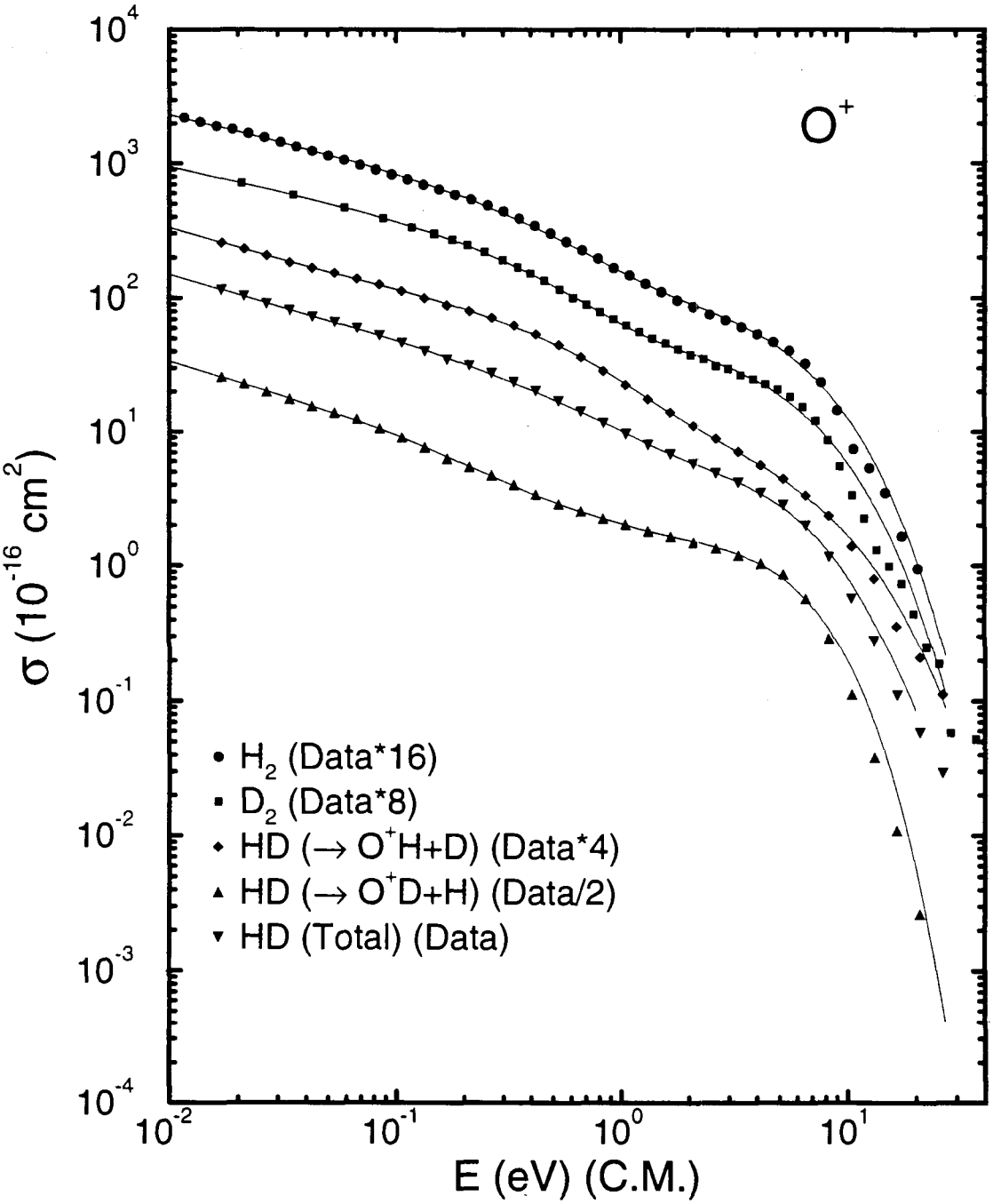

Figure 4: Cross sections for reaction of O^+ with H_2, D_2 and HD as a function of relative kinetic energy. For clarity of presentation the H_2 data and fit are multiplied by 16, the D_2 by 8, and the HD channels by 4 and 1/2 respectively. The lines show the analytic fits with the coefficients given in Table 1.

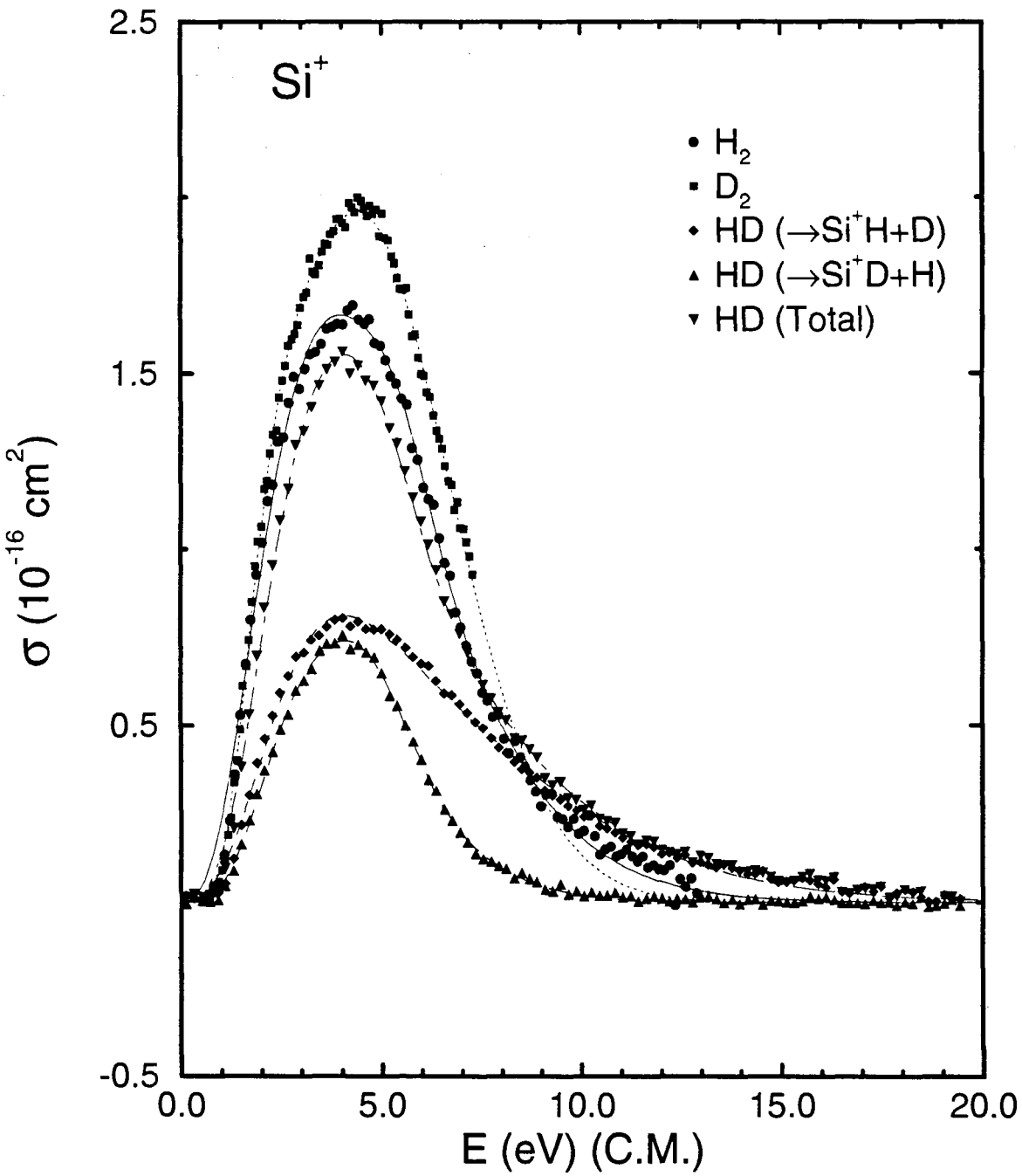

Figure 5: Cross sections for reaction of Si^+ with H_2, D_2 and HD as a function of relative kinetic energy. The lines show the analytic fits with the coefficients given in Table 1.

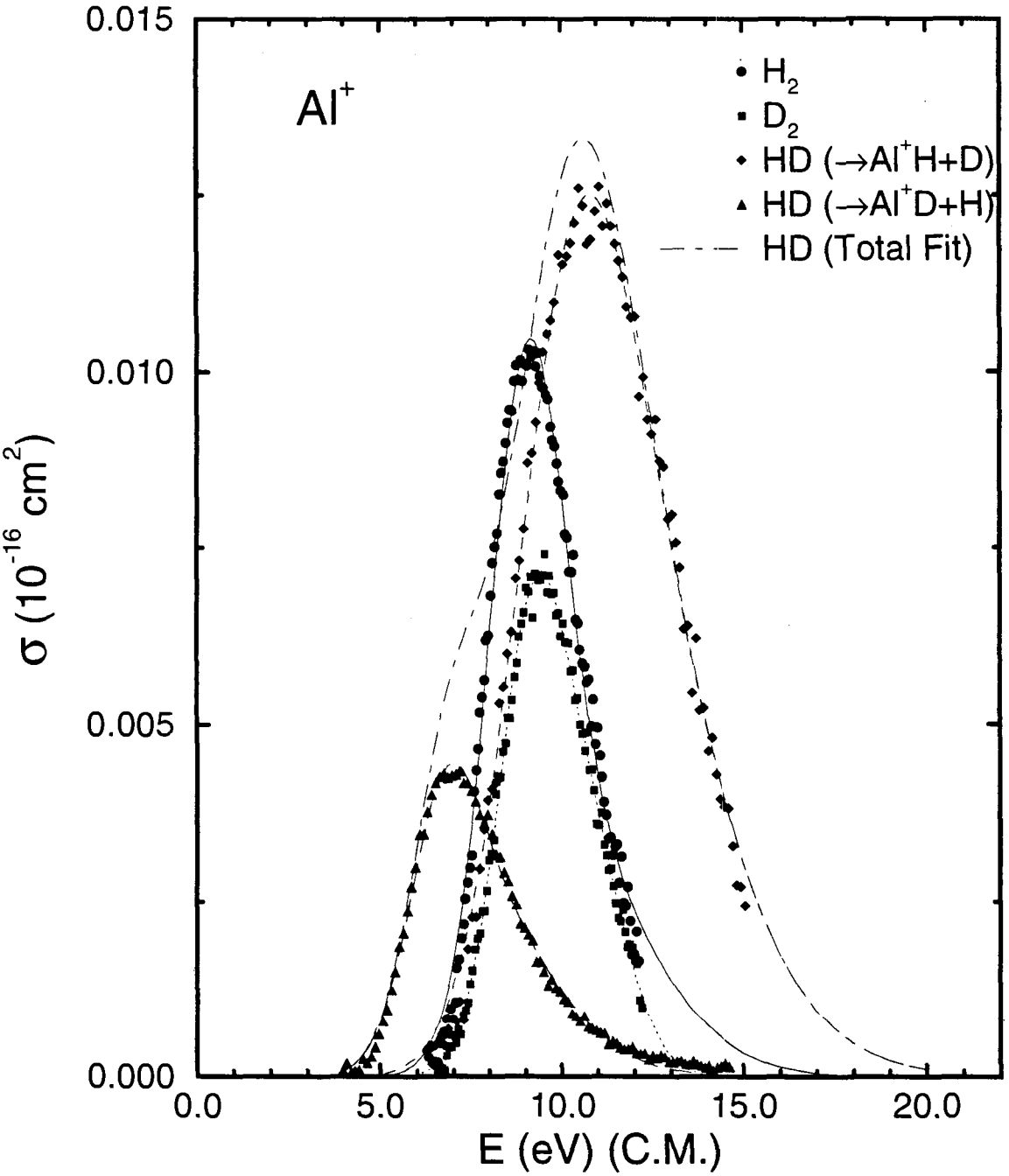

Figure 6: Cross sections for reaction of Al^+ with H_2, D_2 and HD as a function of relative kinetic energy. The lines show the analytic fits with the coefficients given in Table 1.

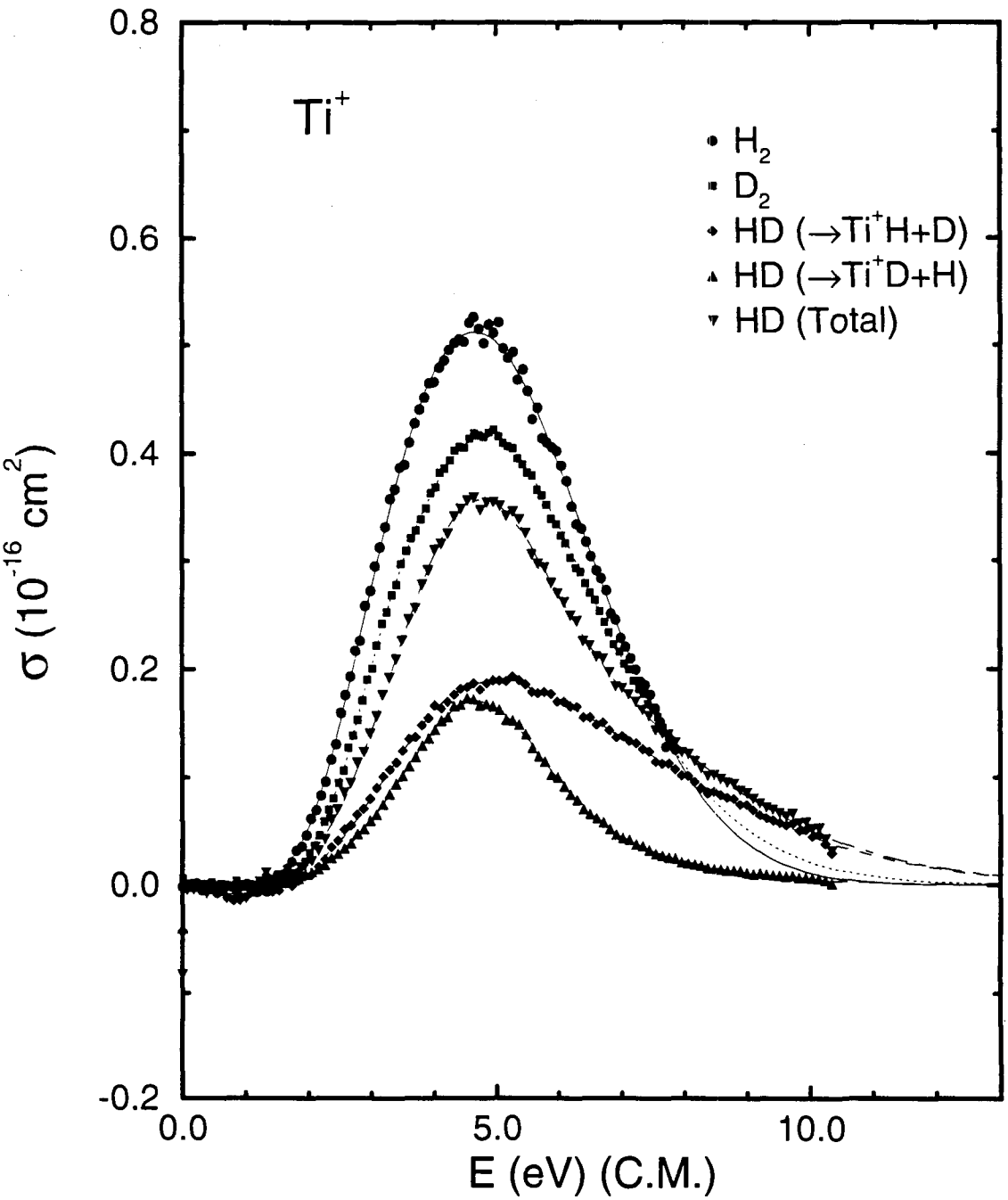

Figure 7: Cross sections for reaction of Ti^+ with H_2, D_2 and HD as a function of relative kinetic energy. The lines show the analytic fits with the coefficients given in Table 1.

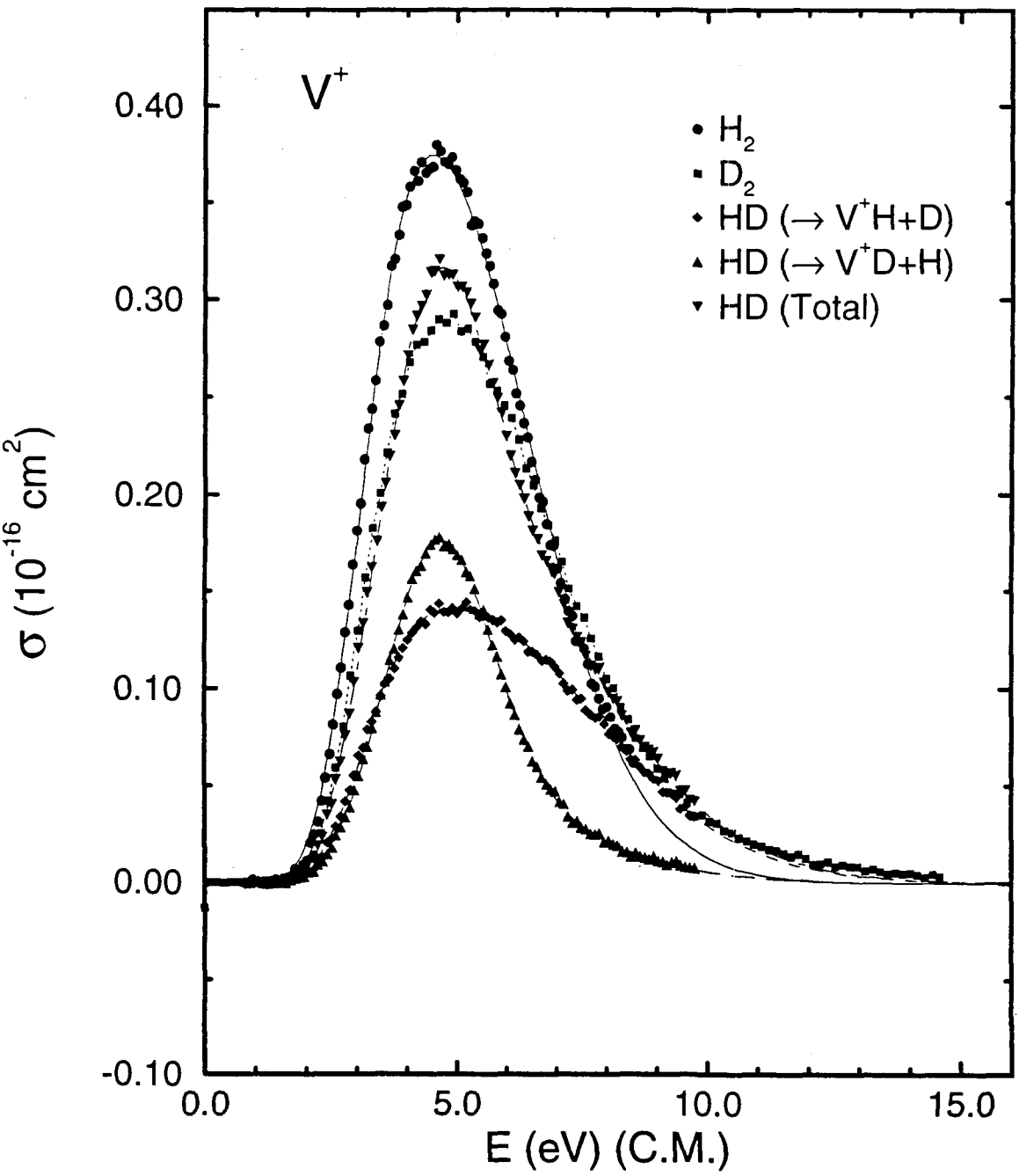

Figure 8: Cross sections for reaction of V^+ with H_2, D_2 and HD as a function of relative kinetic energy. The lines show the analytic fits with the coefficients given in Table 1.

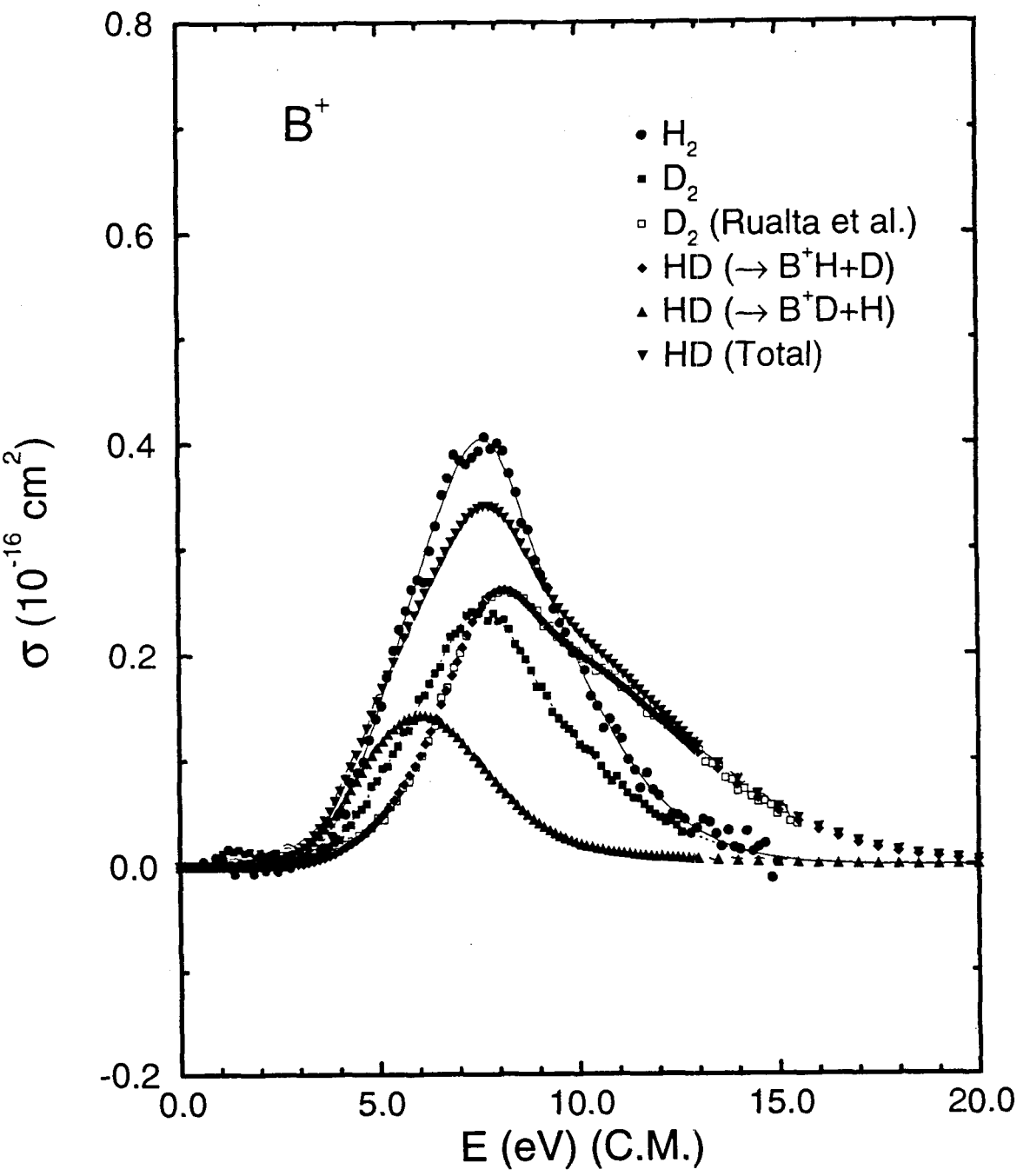

Figure 9: Cross sections for reaction of B^+ with H_2, D_2 and HD as a function of relative kinetic energy. The lines show the analytic fits with the coefficients given in Table 1.

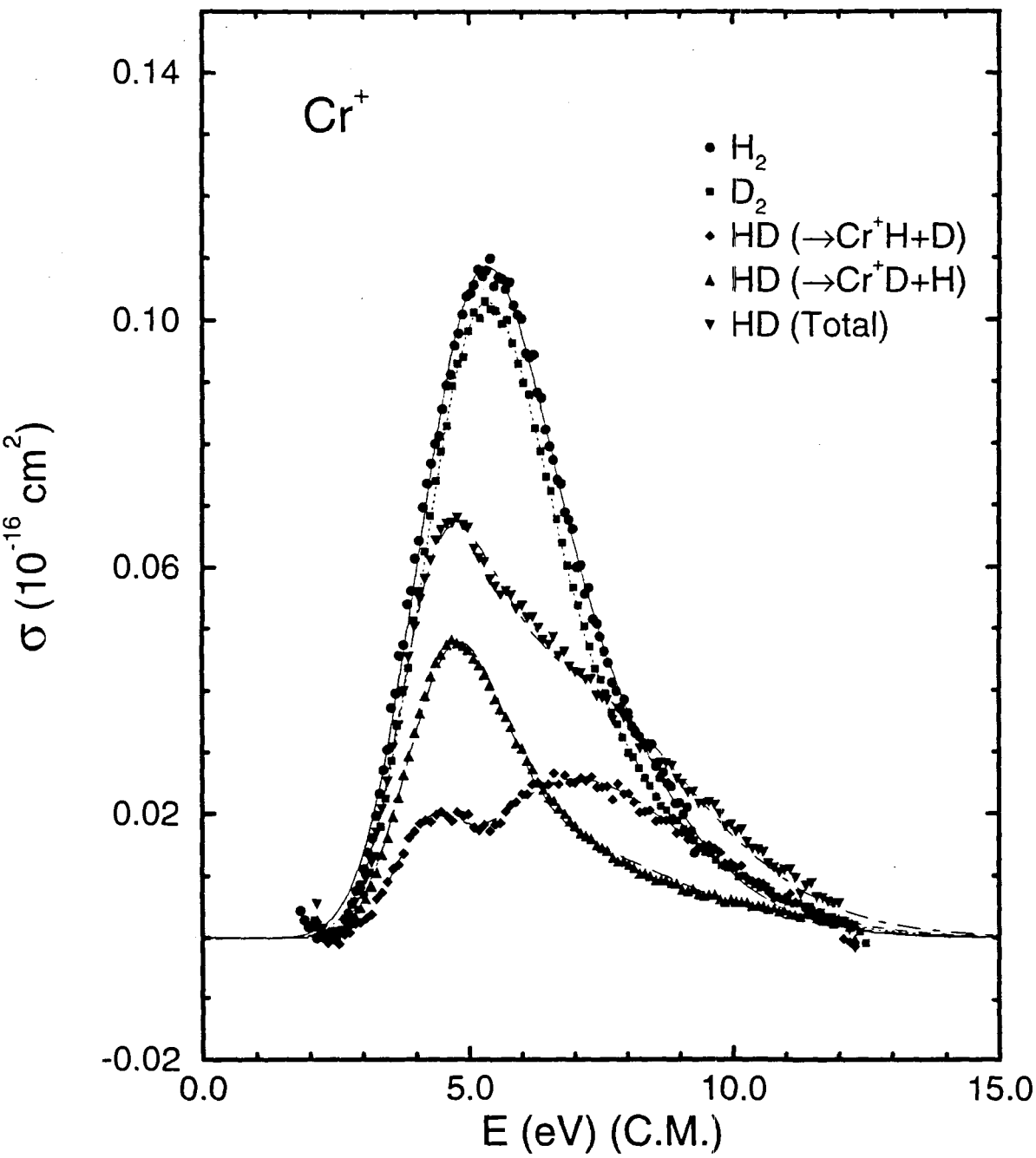

Figure 10: Cross sections for reaction of Cr^+ with H_2, D_2 and HD as a function of relative kinetic energy. The lines show the analytic fits with the coefficients given in Table 1.

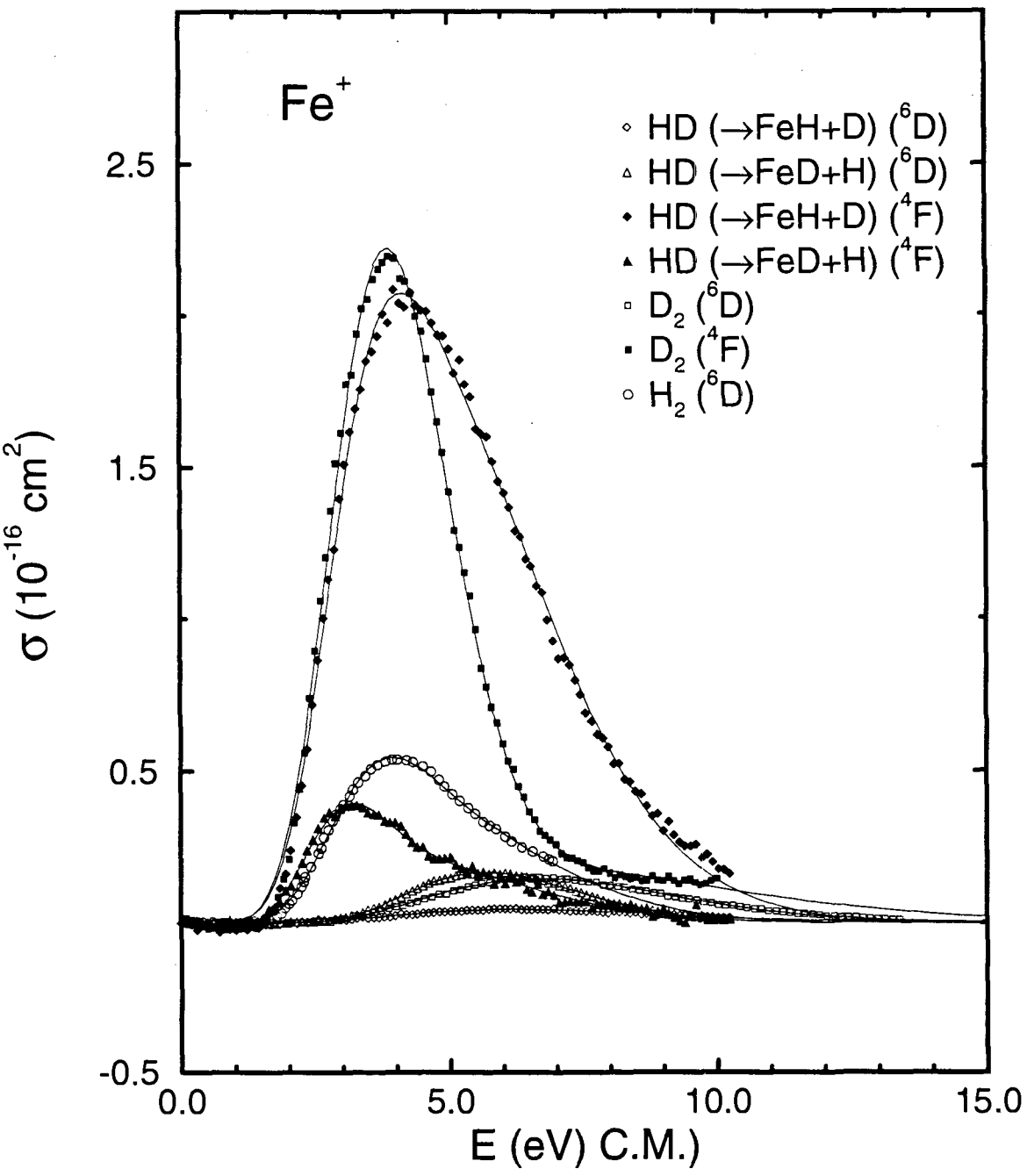

Figure 11: Cross sections for reaction of $Fe^+(^4F$ and $^6D)$ with H_2 (^6D only), D_2 and HD as a function of relative kinetic energy. The lines show the analytic fits with the coefficients given in Table 1.

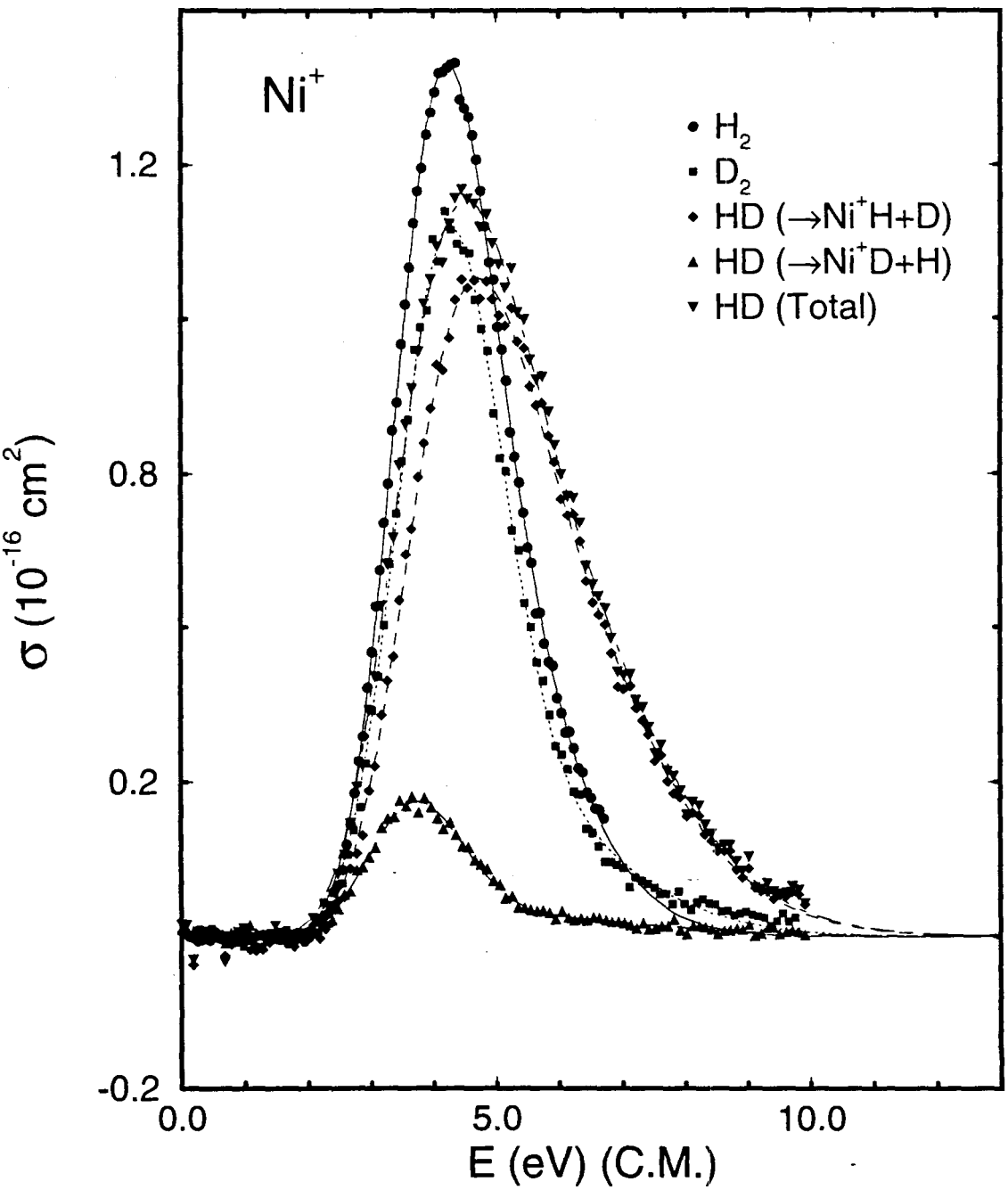

Figure 12: Cross sections for reaction of Ni^+ with H_2, D_2 and HD as a function of relative kinetic energy. The lines show the analytic fits with the coefficients given in Table 1.

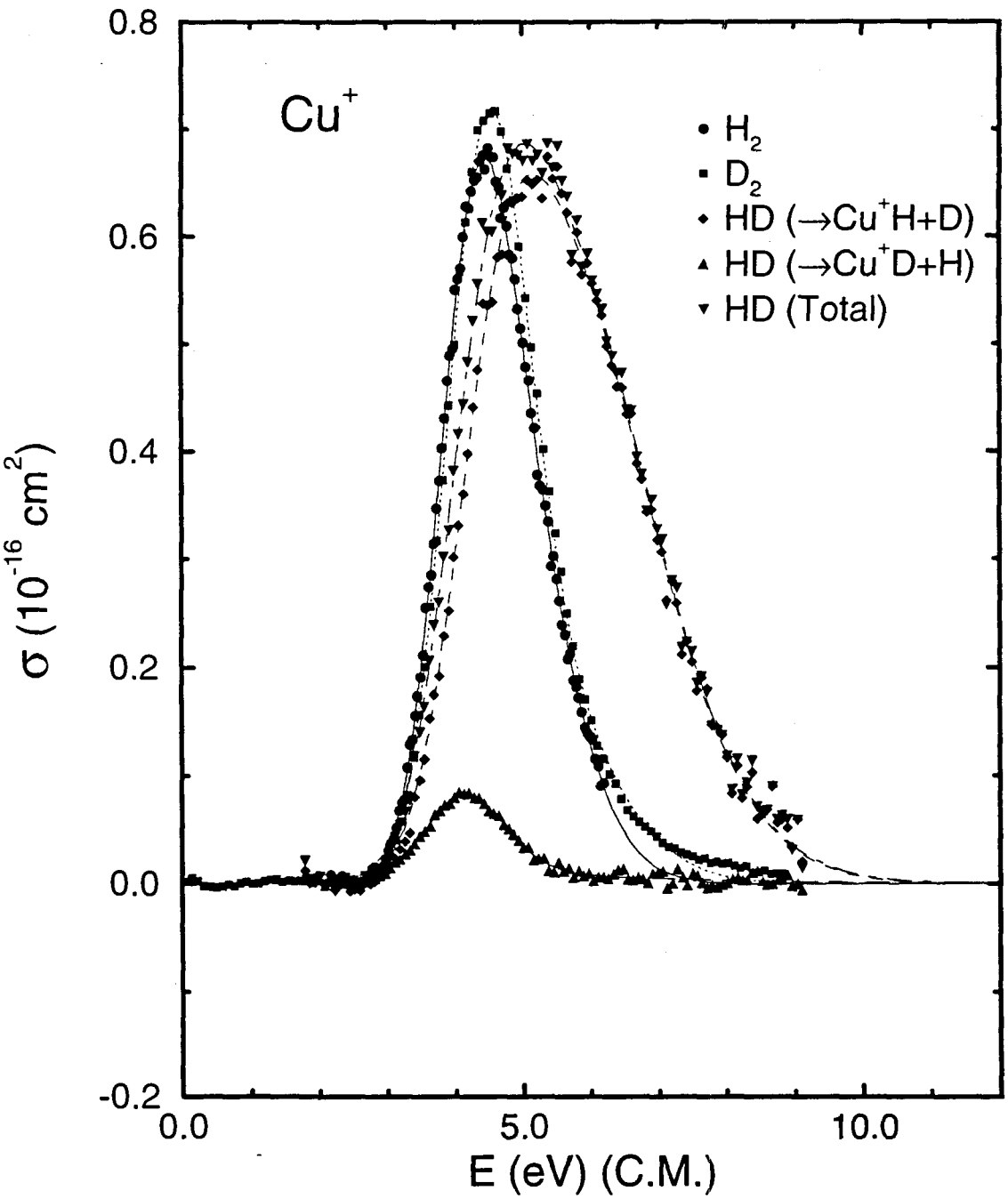

Figure 13: Cross sections for reaction of Cu^+ with H_2, D_2 and HD as a function of relative kinetic energy. The lines show the analytic fits with the coefficients given in Table 1.

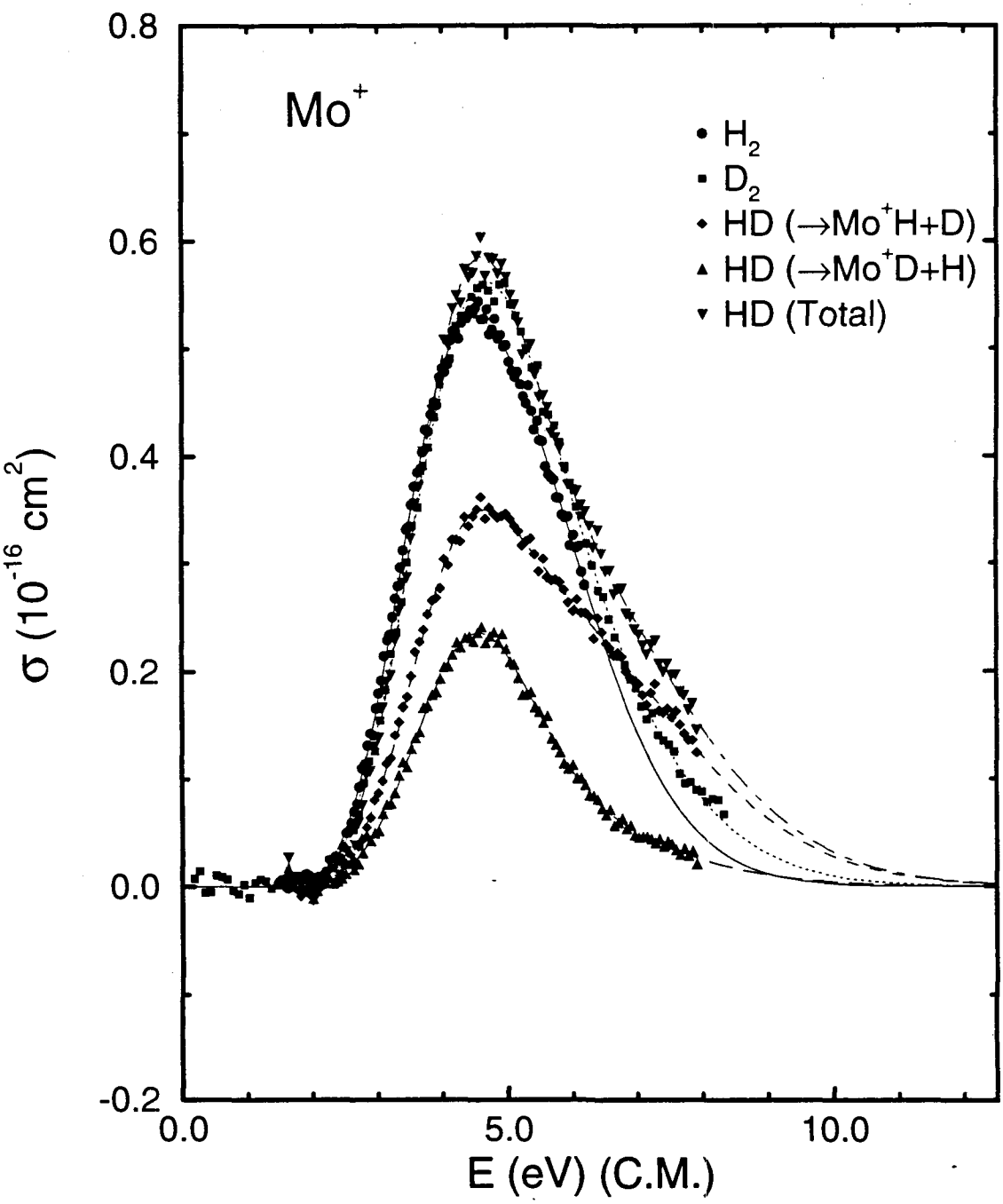

Figure 14: Cross sections for reaction of Mo^+ with H_2, D_2 and HD as a function of relative kinetic energy. The lines show the analytic fits with the coefficients given in Table 1.

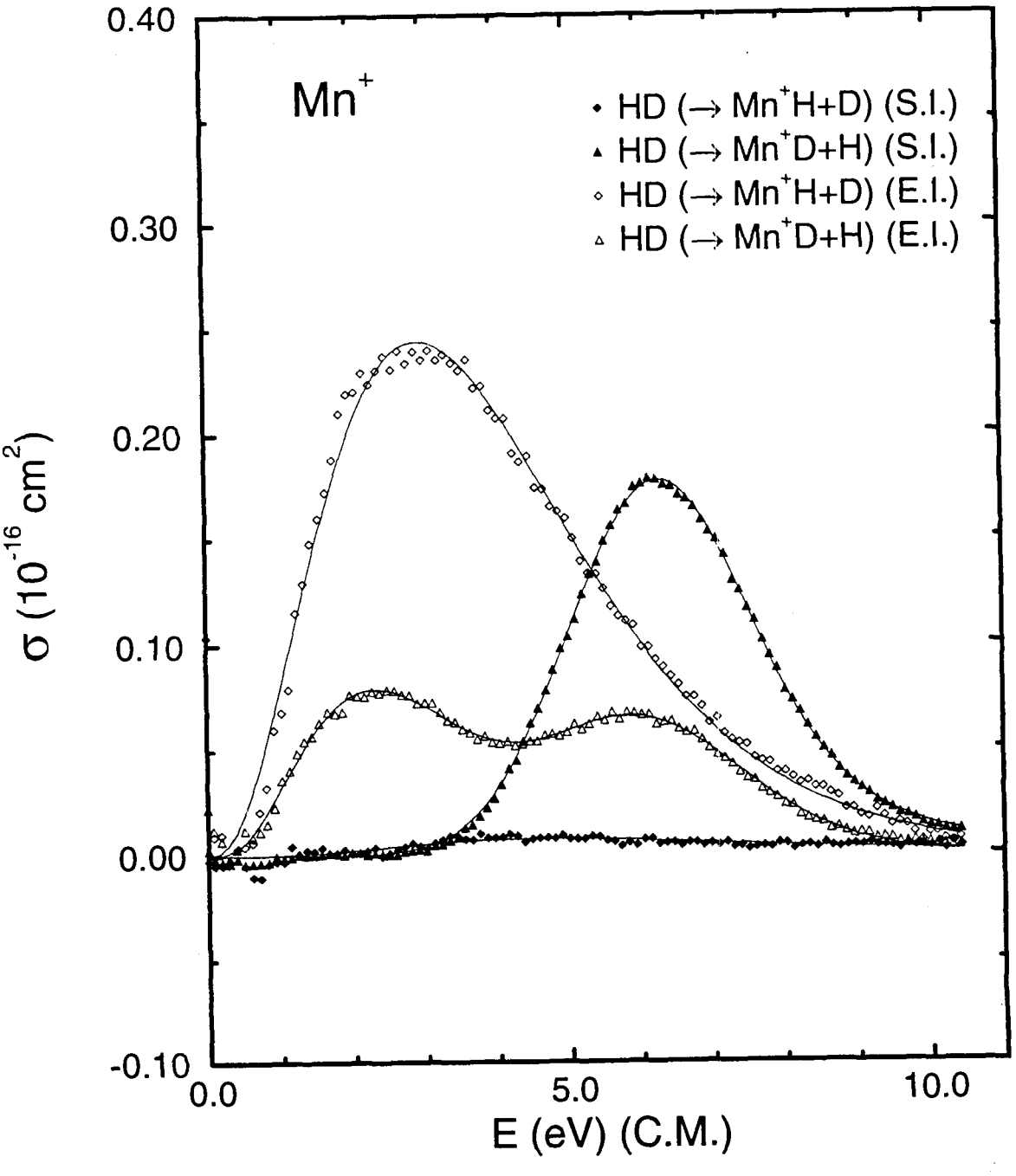

Figure 15: Cross sections for reaction of Mn^+ produced by surface ionization (S.I.) and electron impact (E.I.) with D_2, as a function of relative kinetic energy. The lines show the analytic fits with the coefficients given in Table 1.

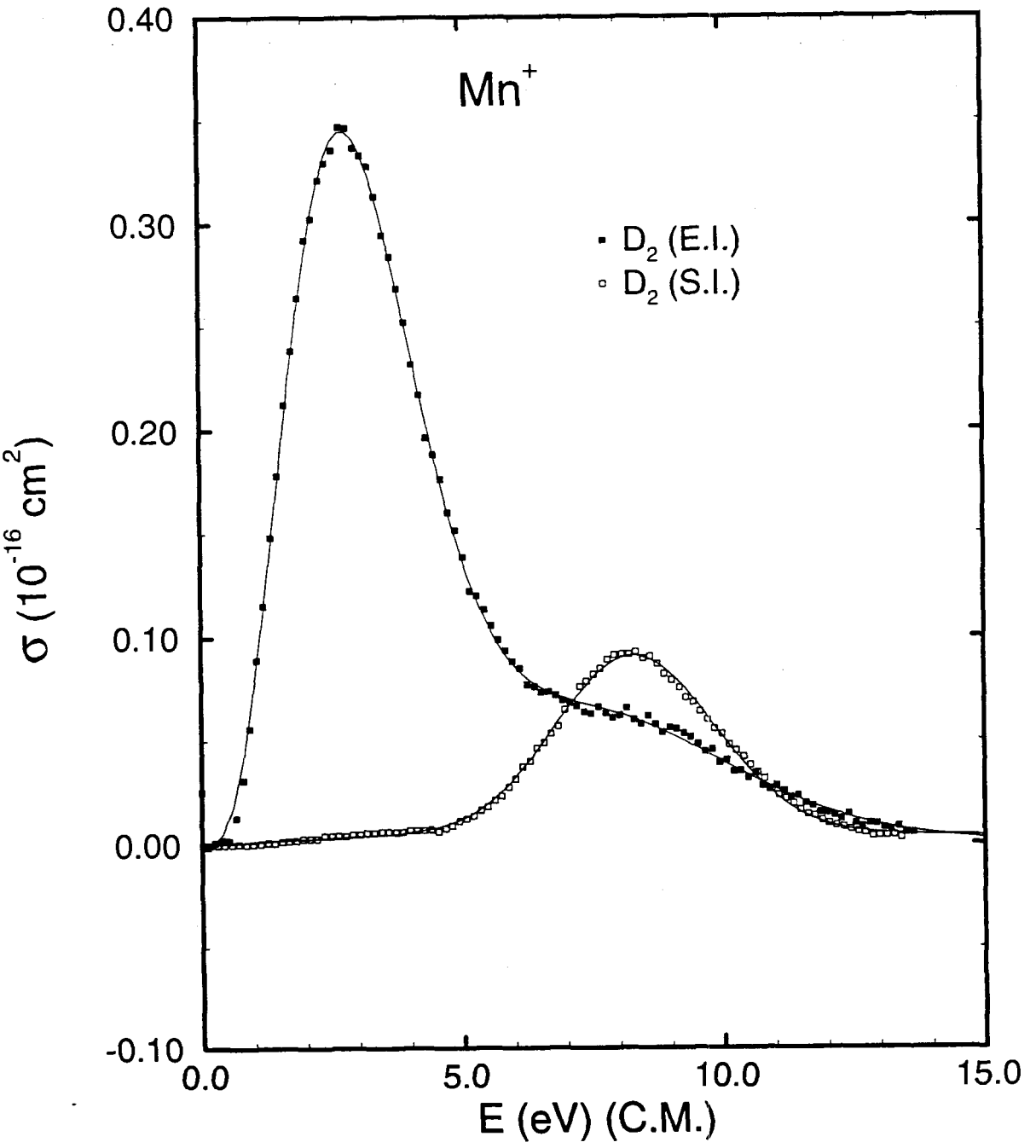

Figure 16: Cross sections for reaction of Mn^+ produced by surface ionization (S.I.) and electron impact (E.I.) with HD as a function of relative kinetic energy. The lines show the analytic fits with the coefficients given in Table 1.

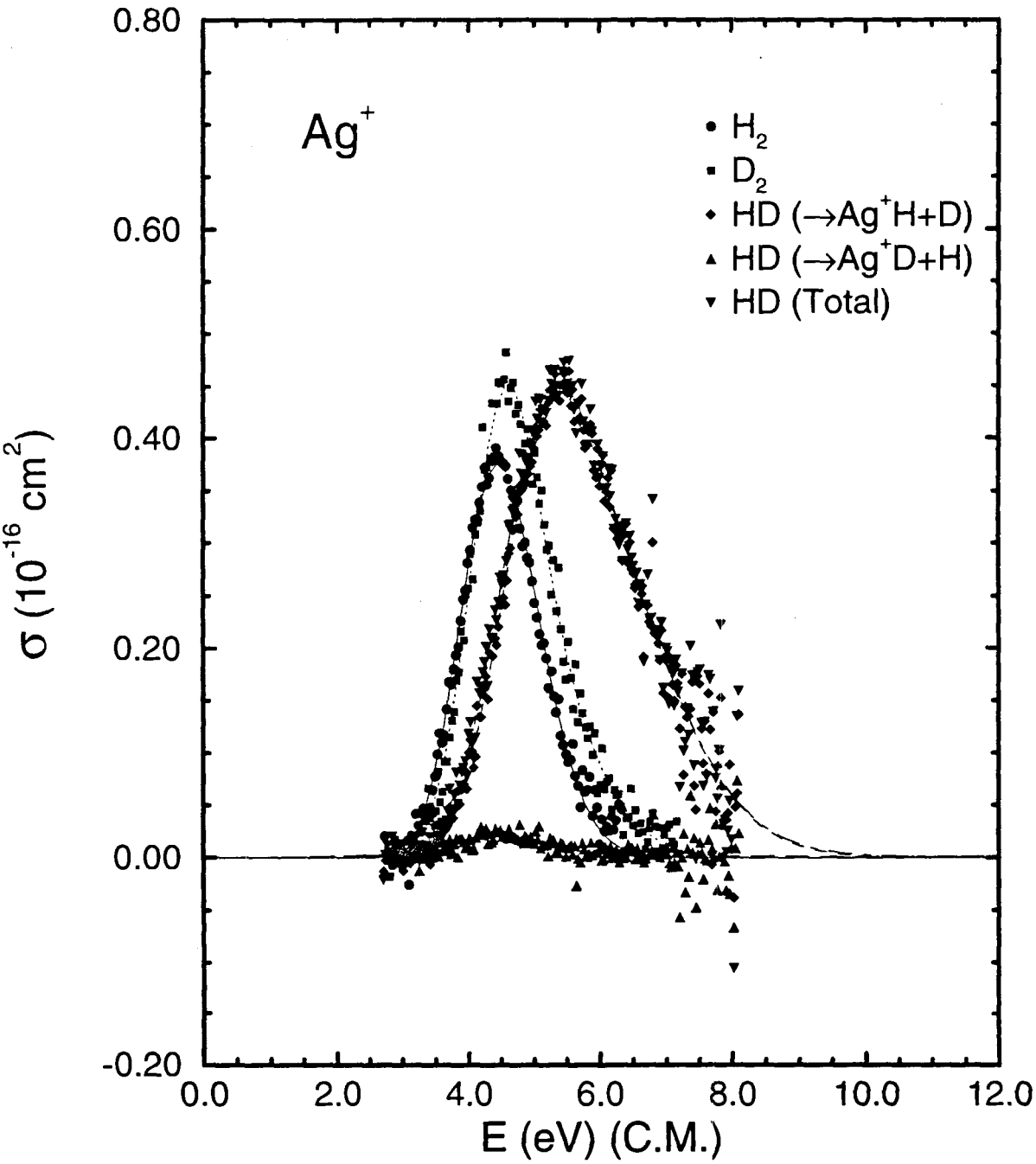

Figure 17: Cross sections for reaction of Ag^+ with H_2, D_2 and HD as a function of relative kinetic energy. The lines show the analytic fits with the coefficients given in Table 1.

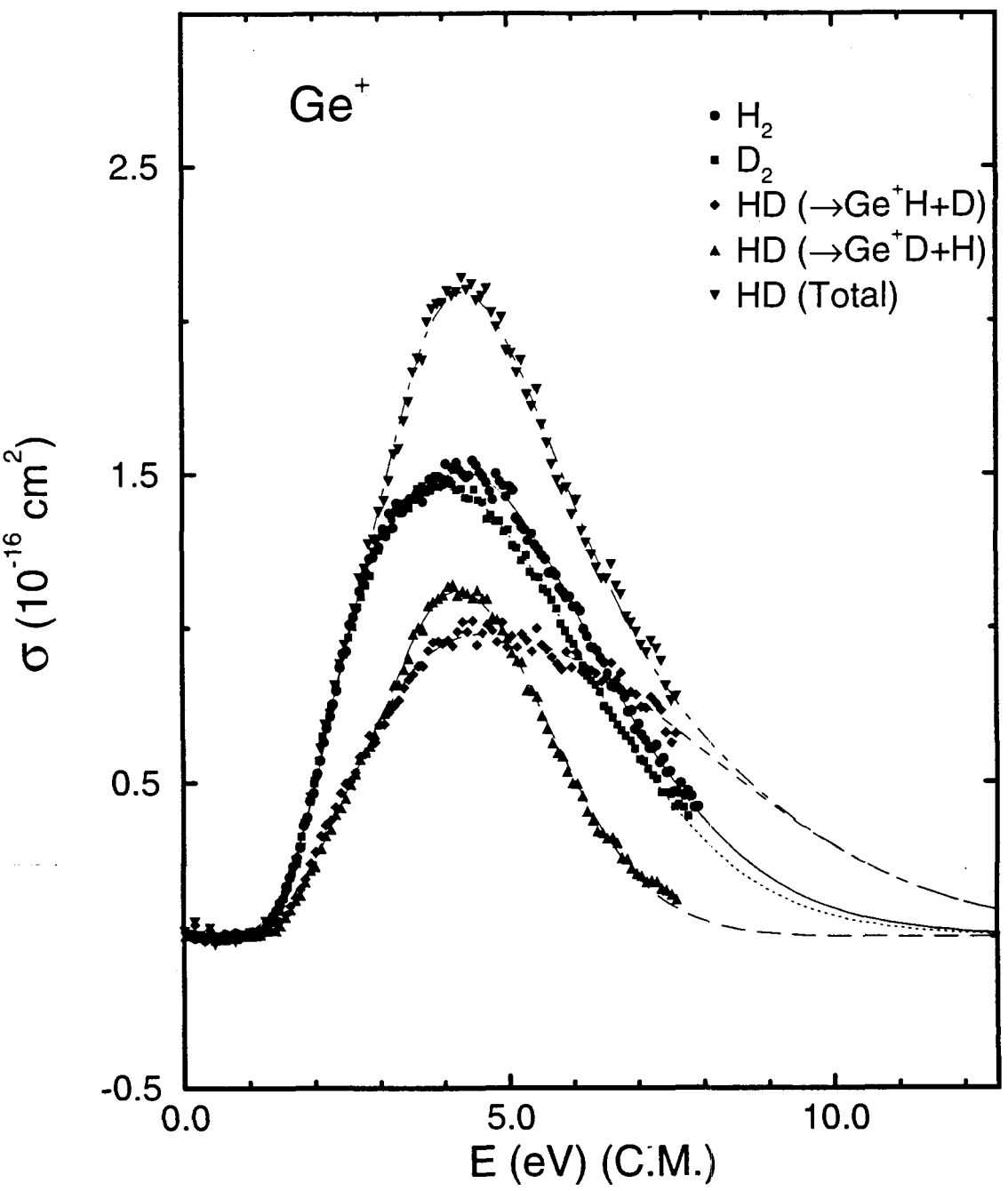

Figure 18 Cross sections for reaction of Ge^+ with H_2, D_2 and HD as a function of relative kinetic energy. The lines show the analytic fits with the coefficients given in Table 1.

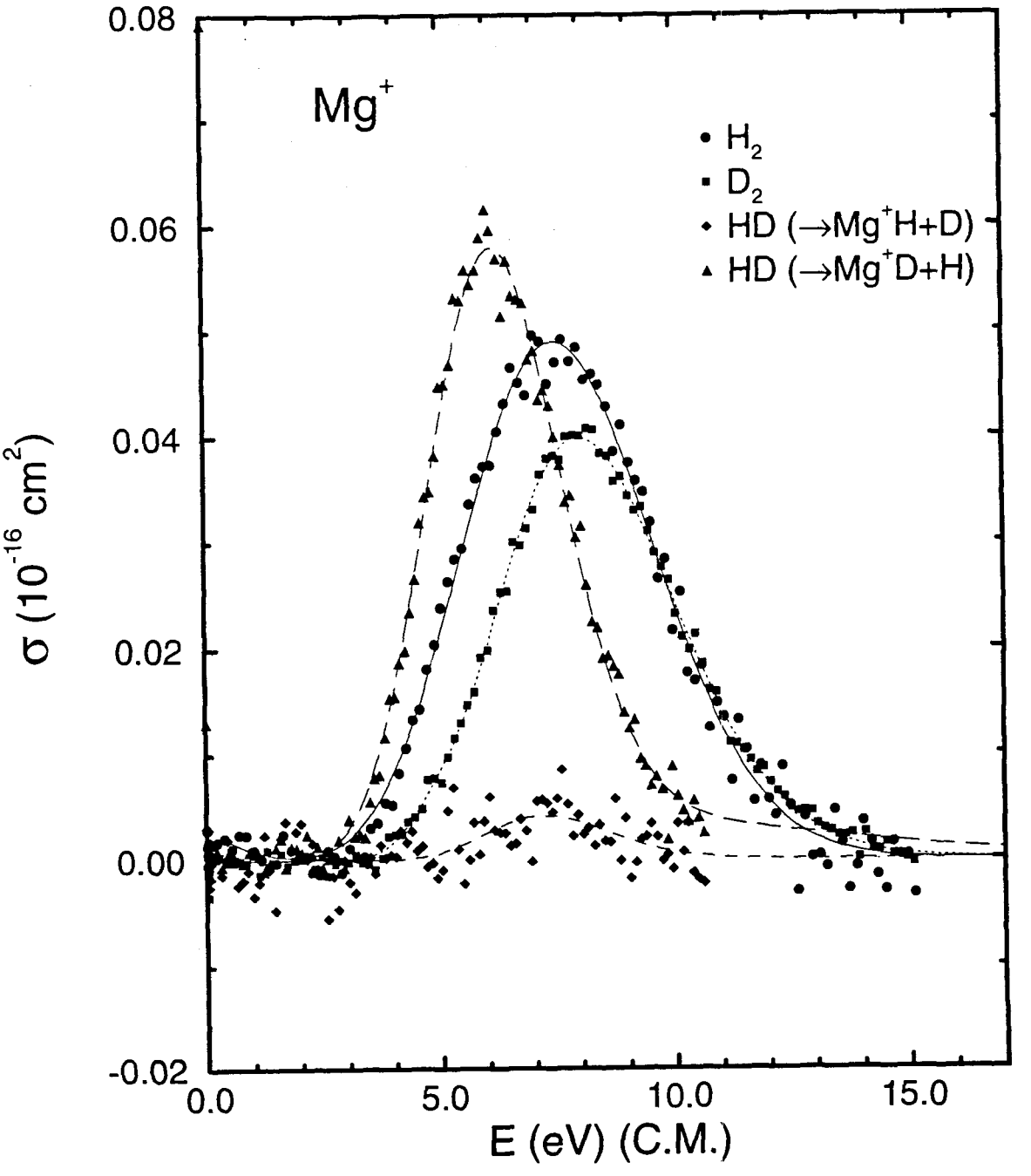

Figure 19: Cross sections for reaction of Mg^+ with H_2, D_2 and HD as a function of relative kinetic energy. The lines show the analytic fits with the coefficients given in Table 1.

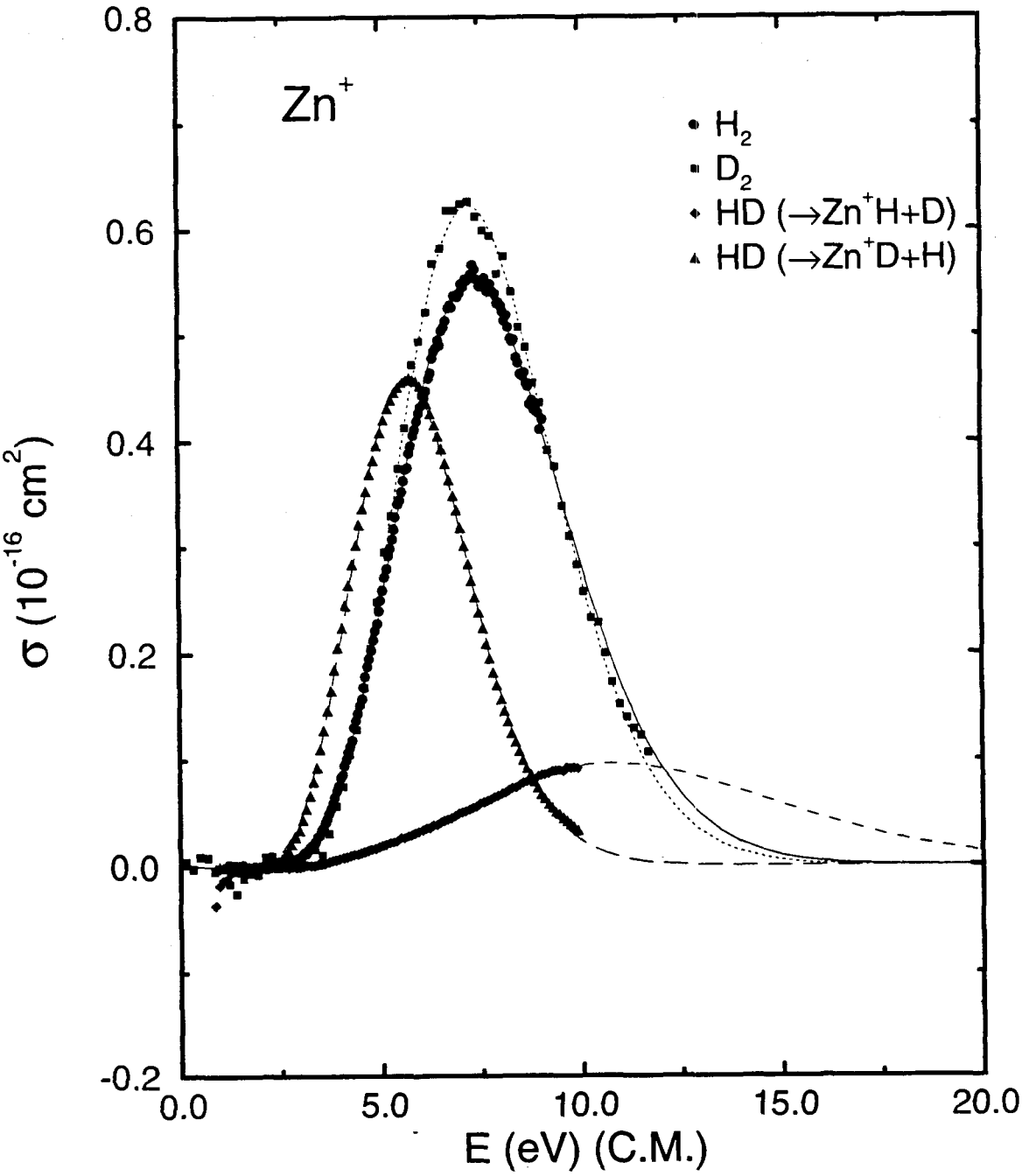

Figure 20: Cross sections for reaction of Zn^+ with H_2, D_2 and HD as a function of relative kinetic energy. The lines show the analytic fits with the coefficients given in Table 1.

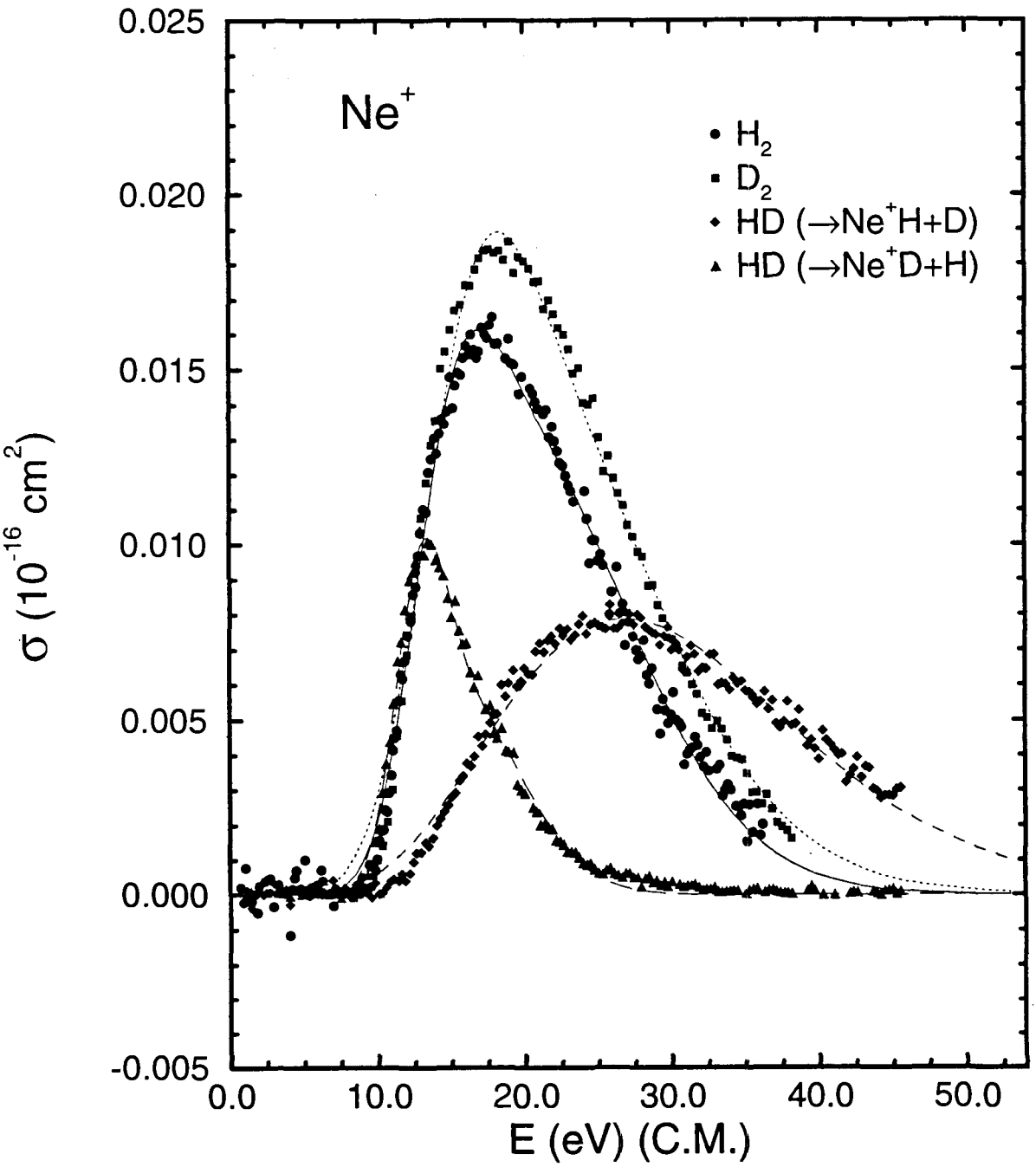

Figure 21: Cross sections for reaction of Ne^+ with H_2, D_2 and HD as a function of relative kinetic energy. The lines show the analytic fits with the coefficients given in Table 1.

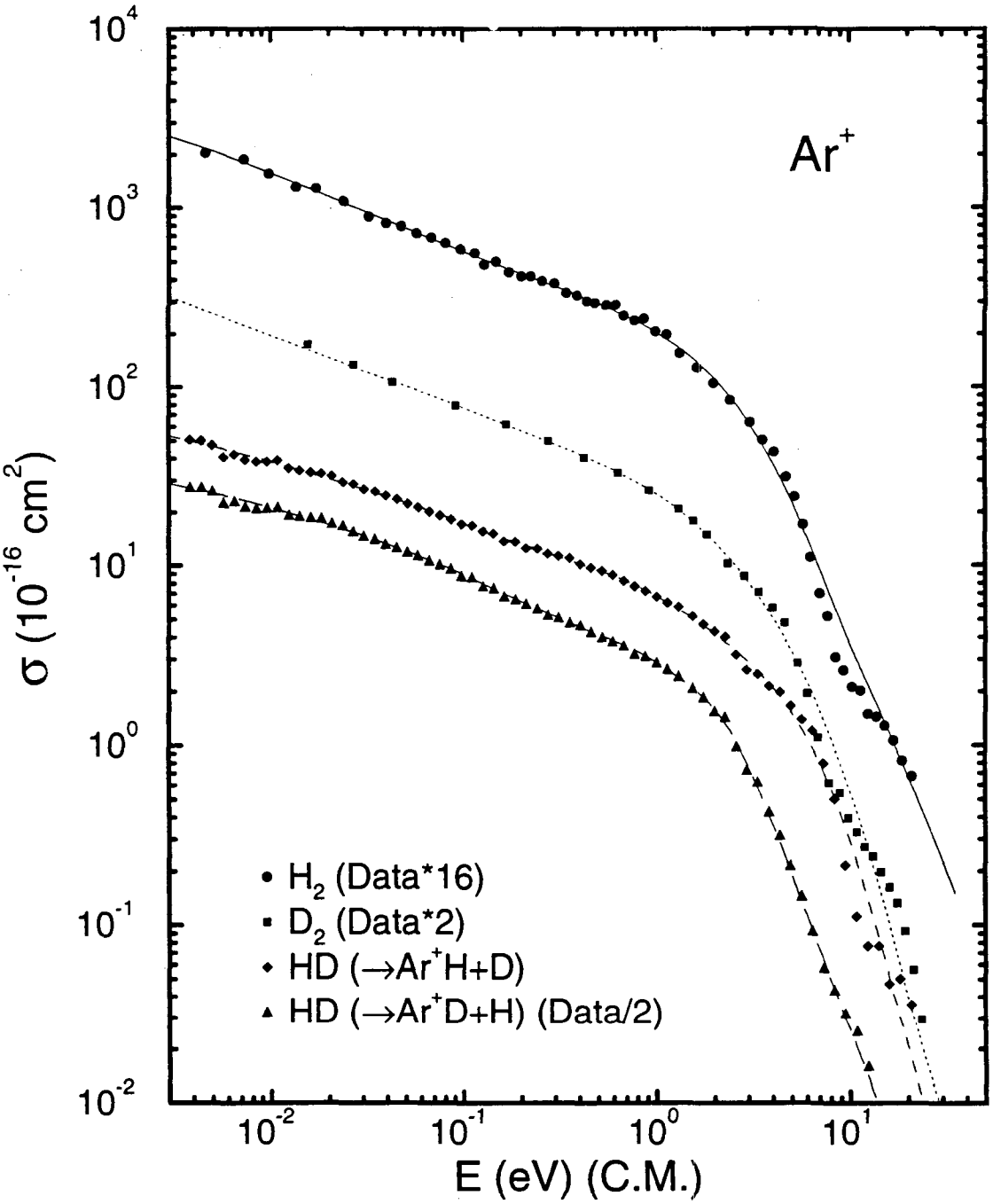

Figure 22: Cross sections for reaction of Ar^+ with H_2, D_2 and HD as a function of relative kinetic energy. The lines show the analytic fits with the coefficients given in Table 1.

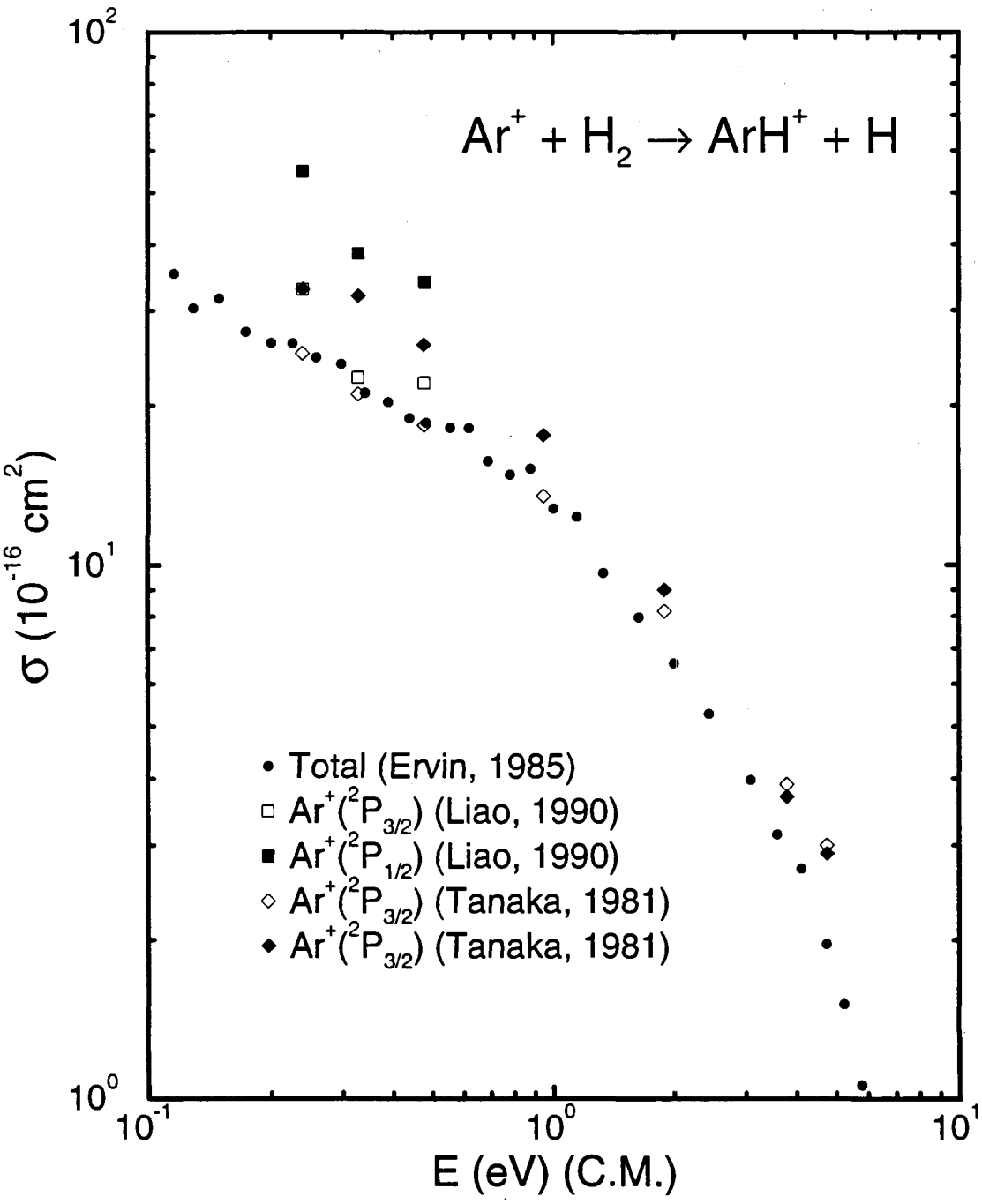

Figure 23: Spin-orbit-state dependence of the cross section for reaction of Ar^+ with H_2.

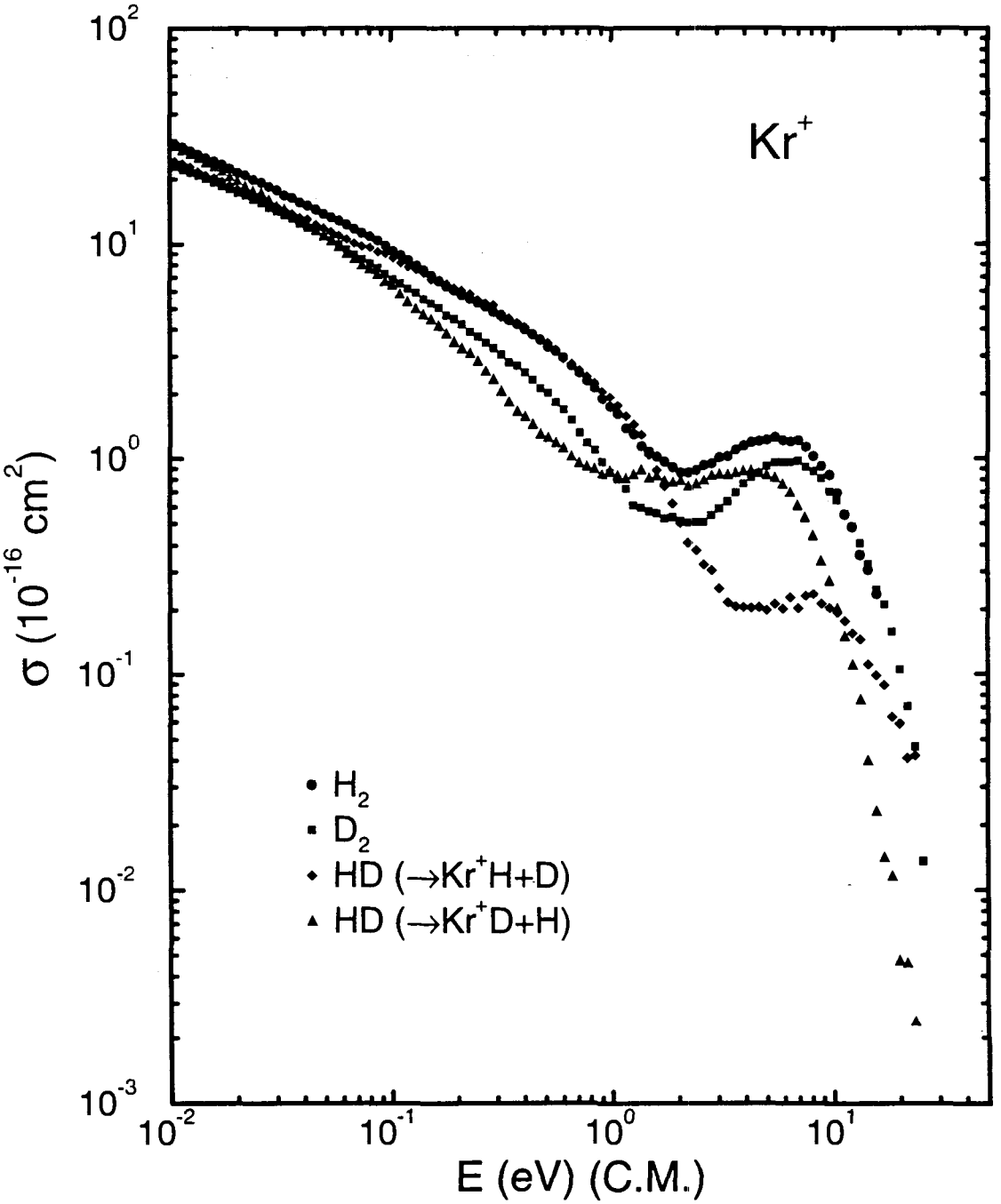

Figure 24: Cross sections for reaction of Kr^+ with H_2, D_2 and HD as a function of relative kinetic energy. The lines show the analytic fits with the coefficients given in Table 1.

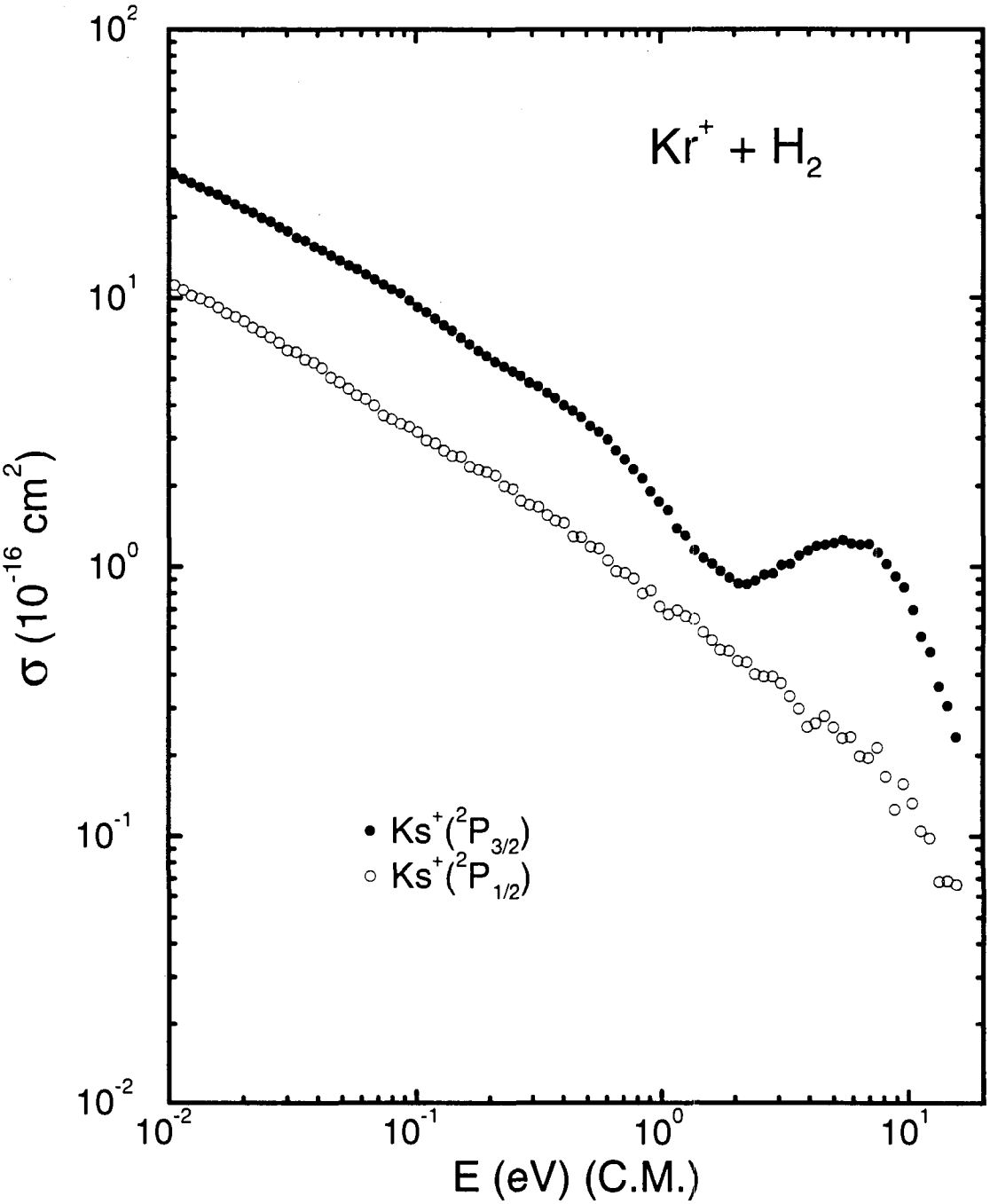

Figure 25: Spin-orbit-state dependence of the cross section for reaction of Kr^+ with H_2.

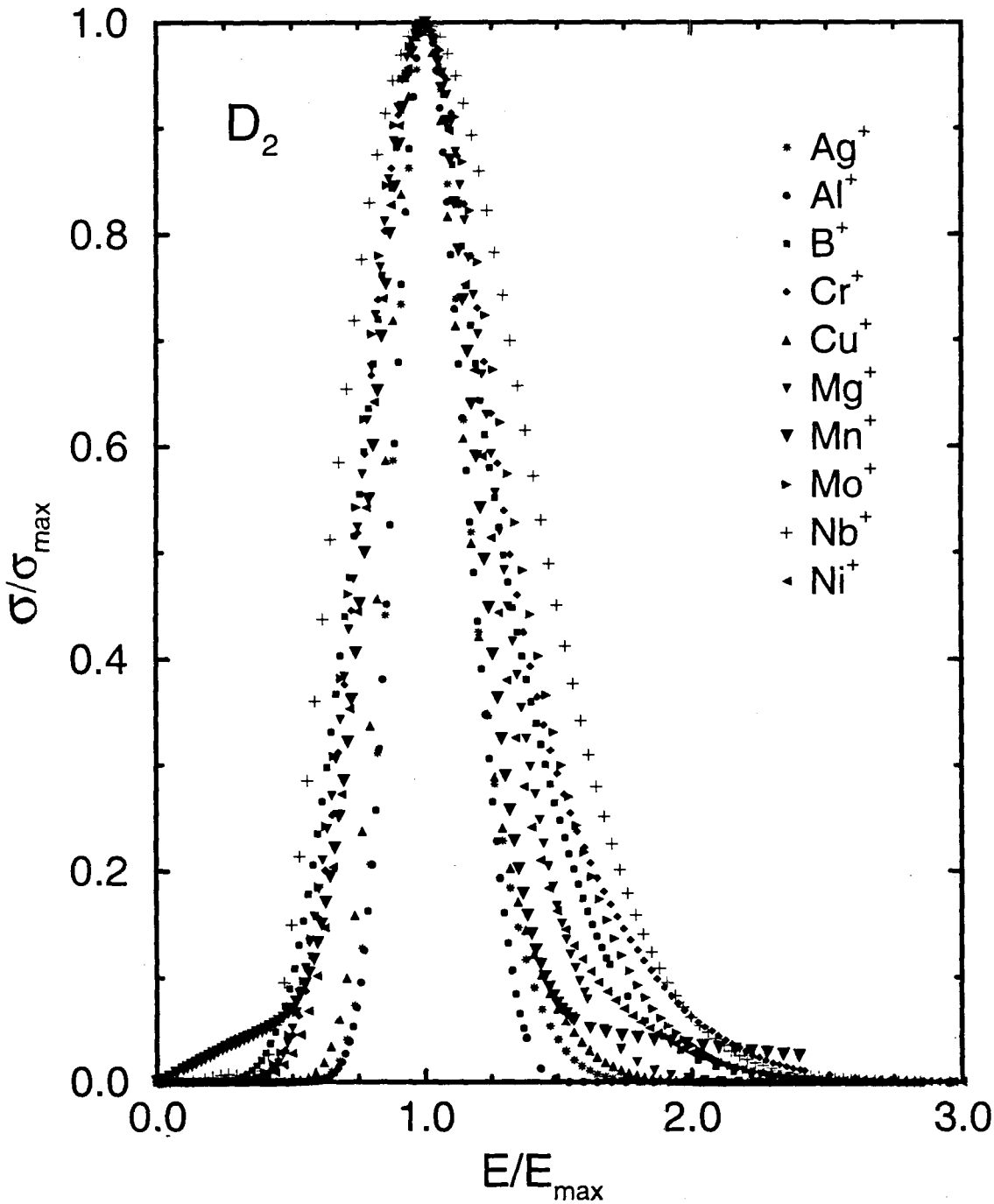

Figure 26: Scaled cross sections for reaction of metals with D_2 as a function of scaled relative kinetic energy (see text).